

Exploring Bifurcations in Bose-Einstein Condensates via Phase Field Crystal Models

A. B. Steinberg,^{1, a)} F. Maucher,^{2, b)} S. V. Gurevich,^{1, 3, c)} and U. Thiele^{1, 3, d)}

¹⁾*Institut für Theoretische Physik, Westfälische Wilhelms-Universität Münster,
Wilhelm-Klemm-Strasse 9, 48149 Münster, Germany*

²⁾*Departament de Física, Universitat de les Illes Balears & IAC-3, Campus UIB,
E-07122 Palma de Mallorca, Spain*

³⁾*Center of Nonlinear Science (CeNoS), Westfälische Wilhelms-Universität Münster,
Corrensstrasse 2, 48149 Münster, Germany*

(Dated: 31 May 2022)

To facilitate the analysis of pattern formation and of the related phase transitions in Bose-Einstein condensates (BECs) we present an explicit approximate mapping from the nonlocal Gross-Pitaevskii equation with cubic nonlinearity to a phase field crystal (PFC) model. This approximation is valid close to the superfluid-supersolid phase transition boundary. The simplified PFC model permits the exploration of bifurcations and phase transitions via numerical path continuation employing standard software. While revealing the detailed structure of the bifurcations present in the system, we demonstrate the existence of localized states. Finally, we discuss how higher-order nonlinearities change the structure of the bifurcation diagram representing the transitions found in the system.

^{a)}ORCID: 0000-0001-6598-9700

^{b)}ORCID: 0000-0002-5808-3967

^{c)}ORCID: 0000-0002-5101-4686

^{d)}ORCID: 0000-0001-7989-9271; Electronic mail: u.thiele@uni-muenster.de; <http://www.uwethiele.de>

The formation of patterns in Bose-Einstein condensates (BECs) has been of great interest in recent years, but their description through nonlinear integro-differential equations makes detailed analyses tedious. An approximation in the vicinity of the superfluid-supersolid phase transition boundary in the form of a phase field crystal (PFC) model allows us to investigate the bifurcation structure and existence regions of different patterns. Of particular interest are localized states, which are commonly investigated for PFC-type models, but have rarely been discussed for Bose-Einstein condensates. Furthermore, we discuss how high-order nonlinearities affect the structure of the underlying transitions.

I. INTRODUCTION

The formation of patterns and structures has always captivated scientists from a broad range of physical disciplines^{1,2} with topics reaching from the dendritic structure of snowflakes³ to patterns of well defined length scales in reaction-diffusion systems or in morphogenesis.⁴ A particular universal model to describe formation of regular patterns in various systems is the Swift-Hohenberg equation.⁵ It was originally formulated for Rayleigh–Bénard convection but also arises in a number of chemical,⁶ ecological⁷ and optical⁸ systems, as well as for elastic materials⁹ to name just a few.

Five decades ago speculations on a quantum state of matter featuring discrete translational symmetry whilst maintaining a large superfluid fraction brought together traditional pattern formation and quantum physics communities.^{10–12} These states of matter are referred to as supersolids. At first, the realisation of such a phase remained elusive. However, recent pioneering experiments^{13,14} involving dipolar Bose-Einstein condensates (BECs) revealed that beyond-mean field contributions describing quantum-fluctuations can lead to a stabilization, a fact that is also true for mixtures of BECs.^{15,16} Ultimately, ultracold dipolar quantum gases turned out to be excellent experimental platform to explore supersolidity.^{13,14,17–24} Here, we take a step back for simplicity and to furthermore complement the discussions on the corresponding dipolar system. In particular, we employ a commonly adopted prototypical toy model of soft-core bosons,^{25–30} which approximates the interaction that is realized when off-resonantly optically coupling to highly excited Rydberg states^{25,31} via Rydberg-blockade.³² Here, we primarily seek to present the method rather than to connect it to specific physical systems.

In order to include supersolidity into the frame of the well-established field of pattern-formation we first derive an approximate mapping valid at the superfluid-supersolid phase transition of the nonlocal Gross-Pitaevskii equation (GPE) to a so-called conserved Swift-Hohenberg (SH) equation, also referred to as phase field crystal (PFC) model,^{33–35} which only involves local nonlinearities (cf. Sec. II). This mapping is sufficiently general to be applicable to other settings involving nonlocal nonlinearities. For example, there are a range of optical systems that are also approximately governed by nonlocal nonlinearities and are suspected to give rise to pattern formation.^{36,37} This idea has already been formulated and explored,³⁸ however, here we propose an alternative mapping that aims at approximating the behavior of the nonlocal GPE close to the phase transition to modulated states.

Our approach permits, on the one hand, the employment of well-established methods for numerical path continuation^{39,40} and, on the other hand, potential synergies of concepts. One such synergy is the concept of localized states that thus far has not yet been explored in depth in the context of BECs. Localized states refer to a situation in which there is a finite patch of one pattern co-existing with a background of another state, often a uniform one. In the context of phase transitions they occur in parameter regions of phase coexistence.^{41,42} Localized states display distinctive features that are independent of the individual examples, such as a bifurcation diagram featuring a snakes-and-ladders structure, alternately referred to as 'homoclinic snaking'.^{43,44} Employing numerical path continuation using, e.g., the package PDE2PATH,⁴⁵ permits one to trace out unstable states as well as stable ones. This allows for a comprehensive exploration of the structure of bifurcation diagrams. As the method is numerically challenging it remains elusive for the nonlocal GPE. Our aim here is to employ it for the local approximation and to explore the advantages and limitations of this approach.

This paper is organized as follows: In Sec. II we start with the mapping of the GPE onto a PFC type model. This is done for an arbitrary interaction in Sec. II A. Next, in Sec. II B, we specify the interaction that is subsequently employed. Sec. II C briefly explains the used numerical methods while Sec. II D discusses the validity of the approximated model for the nonlocal GPE. Sec. III presents bifurcation diagrams for one- and two-dimensional systems including branches of stable and unstable patterned and localized states. In Sec. IV we add a higher order nonlinearity to the model and subsequently discuss linear stability (Sec. IV A) as well as the resulting changes in the bifurcation diagram (Sec. IV B). Finally, in Sec. V, we summarize and conclude.

II. MAPPING THE NONLOCAL GPE TO A PFC MODEL

A. Governing Equations and Mapping

On the mean-field level the dynamics of a BEC is described by a nonlocal GPE for a complex scalar field $\Psi = \Psi(\mathbf{r}, t)$, where the long-range interaction between the bosons gives rise to a convolution. The nonlocal GPE can be written in rescaled form as^{46,47}

$$i\partial_t\Psi = \left(-\frac{1}{2}\Delta + \int d\mathbf{r}' |\Psi(\mathbf{r}')|^2 R(\mathbf{r} - \mathbf{r}') \right) \Psi. \quad (1)$$

Here, R reflects both, long-range interatomic interactions and short-range interactions due to s-wave scattering. As only the product between the amplitude of R (i.e., the interaction strength) and the density $|\Psi|^2$ enters, one can absorb the amplitude of the long-range part of R into the mean density. Therefore, throughout this paper we use $\bar{\rho} = \frac{1}{V} \int |\Psi|^2 d^n r$ as a free parameter.

We would like to approximate Eq. (1) around the phase transition in a way that does not involve a convolution. To approach this problem let us start by writing the corresponding dispersion relation (or excitation spectrum in the superfluid phase),⁴⁸ given by

$$\omega^2(k) = \frac{k^2}{2} \left(\frac{k^2}{2} + 2\bar{\rho}\hat{R}(k) \right), \quad (2)$$

where $\hat{R}(k)$ is the Fourier transform of $R(\mathbf{r} - \mathbf{r}')$. We expect the dispersion relation to show a classical “maxon-roton structure”, i.e., starting from $\omega = 0$ at $k = 0$ it first has a maximum, the “maxon”, and then a minimum, also called “roton minimum” (see, e.g., Fig. 1 (a)). The roton minimum indicates the onset of linear instability for the uniform state as at the corresponding wave number the dispersion relation first crosses zero.

We can introduce the critical values $\bar{\rho}_c$ and k_c , corresponding to the linear stability threshold of the uniform state via $\omega^2(k_c) = 0$ and $\frac{\partial\omega^2}{\partial k}\Big|_{k=k_c} = 0$. Our goal is to match approximately the given dispersion relation Eq. (2) at the phase transition $(k_c, \bar{\rho}_c)$ using a Taylor series $\hat{R}^{(T)}(k)$:

$$\hat{R}^{(T)}(k) = g_0 + g_2 k^2 + g_4 k^4 \quad (3)$$

with the corresponding dispersion relation

$$\omega^{2(T)} = \frac{k^2}{2} \left(\frac{k^2}{2} + 2\bar{\rho}\hat{R}^{(T)} \right). \quad (4)$$

In analogy, one can introduce $k_c^{(T)}$ via $\omega^{2(T)}(k_c^{(T)}) = 0$ and $\frac{\partial\omega^{2(T)}}{\partial k}\Big|_{k=k_c^{(T)}} = 0$. To proceed we have to fix the three free parameters (g_0, g_2, g_4) in an appropriate manner. As we want to approximate

the behavior close to the linear stability threshold a reasonable request for the function $\omega^{2(T)}$ is that it should feature the same critical wavenumber k_c , the same critical density $\bar{\rho}_c$, and the same curvature in the roton minimum $\frac{\partial^2 \omega^2}{\partial k^2} \Big|_{k=k_c}$. This can be realized by solving the set of equations given by

$$k_c = k_c^{(T)}, \quad (5)$$

$$\bar{\rho}_c = \bar{\rho}_c^{(T)}, \quad (6)$$

$$\frac{\partial^2 \omega^2}{\partial k^2} \Big|_{k=k_c} = \frac{\partial^2 \omega^{2(T)}}{\partial k^2} \Big|_{k=k_c^{(T)}}. \quad (7)$$

Independently of the specifics of the long-range interaction, the formal solution of this set is given by

$$\begin{aligned} g_0 &= \frac{k_c^2 \partial_{kk} \hat{R}(k_c) - 2\hat{R}(k_c)}{8}, \\ g_2 &= -\frac{2g_0 - \hat{R}(k_c)}{k_c^2} = -\frac{k_c^2 \partial_{kk} \hat{R}(k_c) - 6\hat{R}(k_c)}{4k_c^2}, \\ g_4 &= \frac{g_0}{k_c^4}. \end{aligned} \quad (8)$$

This differs from the approach in Ref. 38, where $\hat{R}(k)$ is approximated based on its form up to the first minimum. These approaches are similar to gradient expansions of the linear term when deriving PFC models⁴⁹ or to the weakly nonlocal limit in the context of optics.⁵⁰

The approximated version of Eq. (1) now reads:

$$i\partial_t \Psi = \left(-\frac{1}{2}\Delta + g_0|\Psi|^2 - g_2\Delta|\Psi|^2 + g_4\Delta^2|\Psi|^2 \right) \Psi. \quad (9)$$

As the set (g_0, g_2, g_4) is fixed by Eq. (8), this equation only depends on the same parameter $\bar{\rho}$ as before and g_0, g_2, g_4 are uniquely determined by the geometry of the potential.

Through a Madelung transformation,^{51,52} $\Psi = \sqrt{\rho}e^{i\varphi}$ and separating real and imaginary parts we can rewrite Eq. (9) in the following fashion:

$$\partial_t \varphi = \left[\frac{\Delta \rho}{4\rho} - \frac{(\nabla \rho)^2}{8\rho^2} - \frac{(\nabla \varphi)^2}{2} - (g_0\rho - g_2\Delta\rho + g_4\Delta^2\rho) \right], \quad (10)$$

$$\partial_t \rho = -\nabla \cdot (\rho \nabla \varphi). \quad (11)$$

An equation for steady states (including the ground states) is obtained employing the ansatz $\varphi = \mu t$, implying $\nabla \varphi = 0$ and $\partial_t \varphi = \mu$. It reads

$$\mu = \left[\frac{\Delta \rho}{4\rho} - \frac{(\nabla \rho)^2}{8\rho^2} - (g_0\rho - g_2\Delta\rho + g_4\Delta^2\rho) \right]. \quad (12)$$

To describe a dissipative approach to these states we follow appendix D.1 of Ref. 38 and employ a dissipative, locally density-conserving dynamics, i.e., we use a continuity equation $\partial_t \rho = -\nabla \cdot \mathbf{j}$ as Eq. (11) but using the flux $\mathbf{j} = \nabla \mu$. The resulting kinetic equation reads

$$\partial_t \rho = \Delta \left[\frac{1}{2} \left(\frac{(\nabla \rho)^2}{4\rho^2} - \frac{\Delta \rho}{2\rho} \right) + (g_0 \rho - g_2 \Delta \rho + g_4 \Delta^2 \rho) \right]. \quad (13)$$

An alternative to the outlined approach to find groundstates is called "complex/imaginary" time evolution (see e.g., Ref. 53), which employs a Wick-rotation $t \rightarrow -it$ and renormalizes of the wavefunction after each propagation step. Note that the resulting Eq. (13) corresponds to a PFC model^{34,35} with an amended energy functional. Then, μ takes the role of a chemical potential.

At this point we rescale the governing equation (13) to obtain the conventional form for conserved SH-type equations – apart from the peculiar form of the nonlinearity – via

$$r \rightarrow r' \sqrt{-\frac{g_2}{2g_4}}, \quad (14)$$

$$t \rightarrow t' \frac{4g_4}{g_2^2}, \quad (15)$$

$$\rho \rightarrow \rho' \frac{(-g_2)}{2}. \quad (16)$$

Using Eqs. (14)-(16) and dropping the primes we find

$$\partial_t \rho = \Delta \left[\frac{(\nabla \rho)^2}{8\rho^2} - \frac{\Delta \rho}{4\rho} + (\alpha_u + 1)\rho + 2\Delta \rho + \Delta^2 \rho \right], \quad (17)$$

where we use the same interaction parameter

$$\alpha_u = \frac{4g_0g_4}{g_2^2} - 1 \quad (18)$$

as in Ref. 38. In the following, α_u will be a crucial parameter, so we add the convenient formula

$$\alpha_u(k_c, \bar{\rho}_c) = \frac{(k_c^2 \partial_{kk} \hat{R}(k_c) - 2\hat{R}(k_c))^2}{(k_c^2 \partial_{kk} \hat{R}(k_c) - 6\hat{R}(k_c))^2} - 1. \quad (19)$$

It stems from Eqs. (8) and directly links Eq. (17) with the original Eq. (1).

For an appropriate mapping it is important to restrict the range of α_u to values that are in the interval $[-1, 0]$. For smaller values, amplitudes become excessively large and lead to unphysical negative densities. For the interactions considered here, $\alpha_u < 0$ follows naturally.

Written in gradient dynamics form, Eq. (17) reads

$$\frac{\partial \rho}{\partial t} = \Delta \frac{\delta F}{\delta \rho}, \quad (20)$$

where the chemical potential is defined as the functional derivative

$$\mu = \frac{\delta F}{\delta \rho} \quad (21)$$

of the free energy functional

$$F[\rho] = \frac{1}{2} \int_V \left[\frac{|\nabla \rho|^2}{4\rho} + (\alpha_u + 1)\rho^2 + 2\rho \Delta \rho + \rho \Delta^2 \rho \right] d^n r. \quad (22)$$

Note, that we use the notion of a "free energy" despite the temperature dependence being suppressed. In our case, it stems from the fact that imposing $\nabla \phi = 0$ for Eq. (12) implies that we consider dissipative pseudo dynamics and adopt the vocabulary of soft-matter physics.

The corresponding grand potential density is Ω/V with

$$\Omega = F - \int \mu \rho d^n r. \quad (23)$$

Both, μ and Ω/V are important for the investigation of the existence of coexisting states at phase transitions.

B. Soft-core Bosons and their Dispersion Relation

In the following, we consider a Heaviside step function $\Theta(1 - r)$ with $r = |\mathbf{r}|$ as prototypical toy model for soft-core interactions^{25,27,28} and a delta function $\delta(r)$ to describe s-wave scattering, hence

$$R(r) = \Theta(1 - r) + a\delta(r). \quad (24)$$

Here, a corresponds to the rescaled scattering length, and the strength of the long-ranged interaction has been absorbed in the mean density. We employ this particularly simple interaction to conveniently illustrate the method. We do not discuss the subject of collapse that can occur for attractive scattering length, as it has been discussed elsewhere in depth.^{54,55} Here, we merely use the scattering length to deform the dispersion relation.

The resulting dispersion relation Eq. (2) and its approximation Eq. (4) are compared in Fig. 1. When evaluating Eqs. (8) it has to be noted that they are implicit expressions: k_c and $\bar{\rho}_c$ depend parametrically on a and have to be found from Eq. (2). We find

$$\hat{R}(k) = \begin{cases} \frac{2 \sin(k)}{k} + a, & 1D \\ 2\pi \frac{J_1(k)}{k} + a, & 2D \end{cases} \quad (25)$$

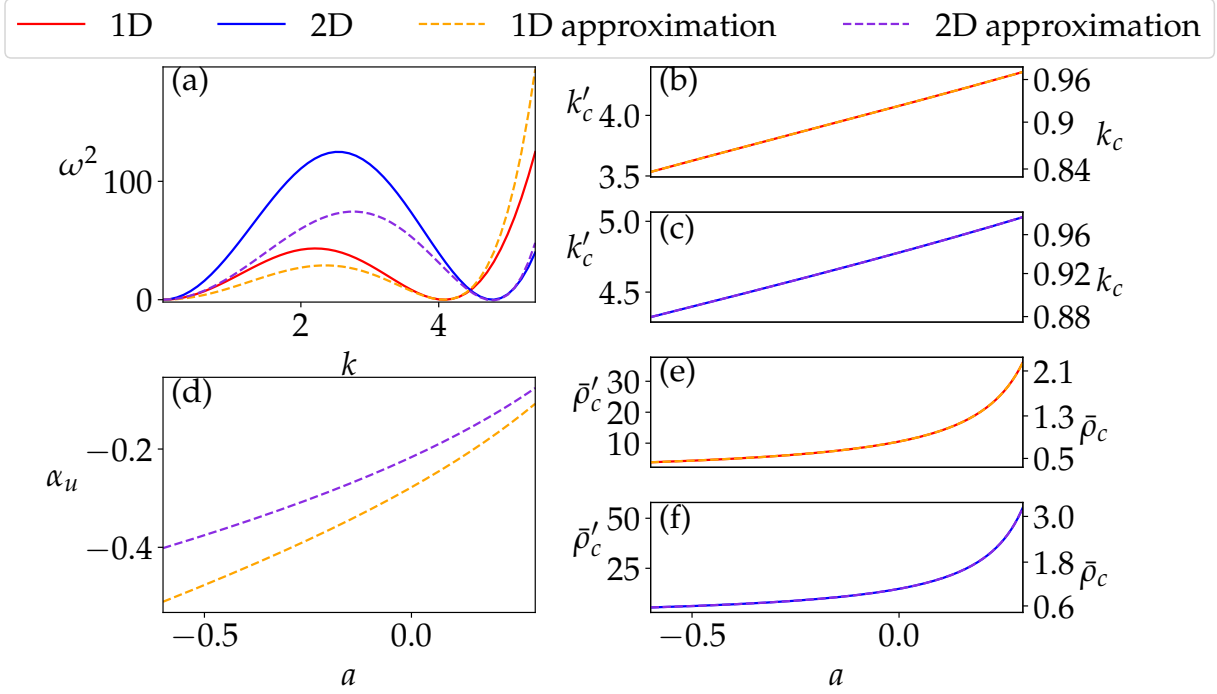


FIG. 1. Comparison between the exact model [Eq. (1)] and its approximation [Eq. (9) or Eq. (17)]. (a) Dispersion relations given by Eq. (2) (solid lines) and the approximation (4) (dashed lines) at the onset of the modulational instability. One- (1D) and two-dimensional (2D) cases are represented in red/orange and blue/purple, respectively (see legend). Also given are the dependencies of the (b-c) critical wavenumber k_c and the (e-f) critical density $\bar{\rho}_c$ on the rescaled scattering length a . Panel (d) shows the dependency of α_u on a . The two axis on the left and right of panels (b,c,e,f) relate to the unscaled and scaled system, respectively. As the scaling is nonlinear for both, $\bar{\rho}_c$ and k_c , the right axis is nonlinear.

where $J_1(k)$ is the Bessel function of the first kind. It is instructive to compare the dispersion relations of the approximated model Eq. (4) and the original model Eq. (2). Figure 1 (a) compares such relations in the cases of one-dimensional (1D) and two-dimensional (2D) systems. By construction, wavenumber k_c and density $\bar{\rho}_c$ perfectly match while features like the curvature at $k = 0$ and characteristics of the maximum deviate. Figures 1 (b) to (f) furthermore show, how k_c , $\bar{\rho}_c$ and α_u depend on the rescaled scattering length a . Before we proceed in the discussion of the validity of the approximated model in section II D, we comment on the employed numerical methods.

C. Numerical Methods

The ground state, i.e., the steady state with minimal energy of the GPE (1) and its approximation [Eq. (9)] can be obtained via direct numerical simulations using Fourier split-step method combined with the so-called complex time evolution. The latter consists in converting the original equation in a diffusion-type equation via a Wick rotation of the time coordinate, $t \rightarrow -it$ and renormalizing the norm after each step. In particular, the Fourier split-step method implies that the corresponding Hamiltonian is split, according to the Baker–Campbell–Hausdorff formula, into a linear kinetic part that is diagonal in Fourier space and a nonlinear part that is diagonal in real space. However, this method only gives access to stable ground states and does not permit calculating unstable any solution branches.

While the results based upon direct numerical integration allow one to obtain basic estimates of the stability range for a generic parameter set, a full bifurcation study of the system is still lacking. In order to track the pertinent states in parameter space we employ numerical pseudo-arclength continuation methods.^{39,40} They trace branches of steady states through parameter space employing a combination of tangent predictor steps and correction steps using Newton’s method. Here, we use path continuation employing the package PDE2PATH.⁴⁵

Normally, we employ periodic boundary conditions (BC) implying a valid continuous translational symmetry. Mean density and phase conservation are enforced via auxiliary conditions. The latter account for the continuous symmetries where the auxiliary conditions prevent a motion along the corresponding group orbit during continuation.⁴⁰ To improve the performance of the path continuation in the 2D case, we choose domain geometry and size that match a specific pattern symmetry. Occasionally, the periodic 2D domain can be further reduced by exploiting the symmetry of the pattern that is traced. For instance, a square pattern in a square domain may be considered in a domain one forth of the original size by employing Neumann BC that also automatically enforce the phase conditions for translation. However, bifurcations which break that symmetry can no longer be detected.

D. Validity of the Approximated Model

In the following, we compute the ground states and their phase transition from uniform to modulated states for $R(r) = \Theta(1 - r)$ (i.e., for $a = 0$) for both, Eq. (1) and Eqs. (9) [or Eq. (17)] to

probe the validity of the approximation. As path continuation now allows us to trace out unstable solutions of the approximated model, we will add them to the bifurcation diagrams as well.

Figure 2 shows the resulting bifurcation diagram for steady states in 1D and 2D in dependence of the mean concentration $\bar{\rho}$. The states are characterized by the contrast

$$C = \frac{\rho_{\max} - \rho_{\min}}{\rho_{\max} + \rho_{\min}}, \quad (26)$$

where zero contrast represents a uniform superfluid state. As expected, the linear stability thresholds exactly agree, e.g., $\bar{\rho}'_c = 10.5$ for the 1D case. Consistently between exact model and approximation, the primary bifurcation at $\bar{\rho}_c$, is supercritical in 1D and subcritical in 2D. In consequence, in 1D the weakly and fully nonlinear behaviors first closely agrees and then quantitatively deviates further from the threshold once the amplitude of the density wave increases. The difference is about 20% at the right hand side end of the diagram in Fig. 2 (a). In the 2D case, the linear stability threshold is at $\bar{\rho}'_c = 14.7$ where the branch of patterned states subcritically emerges, leading to a region of bistability (not to be confused with thermodynamic coexistence which would indicate localized states). Note that the unstable states on the subcritical part of the branch can be obtained by path-continuation but not by time simulation. Here, we are only able to employ continuation for the approximate, i.e., local model, but not for the exact, i.e., nonlocal model. For the latter we can only employ time simulations to calculate stable states, i.e., the states beyond the stabilizing saddle-node bifurcation. Therefore, the subcritical part where we expect good agreement unfortunately can not be compared. As the saddle-node bifurcation occurs in the fully nonlinear regime, there is an appreciable deviation (of about 10% in absolute terms) between its positions in the exact and approximate model [see Fig. 2 (b)]. Note, that Ref. 49 also points out several closely related consequences of applying such an approximation to dynamic density functional theory, such as changes to the phase boundaries and regions without physical solutions.

III. PERIODIC PATTERNS AND LOCALIZED STATES

In this section we will explore different types of periodic patterns as well as localized states supported by the approximated model (9) mainly in the 2D case. However, we will start with a brief discussion of the 1D case.

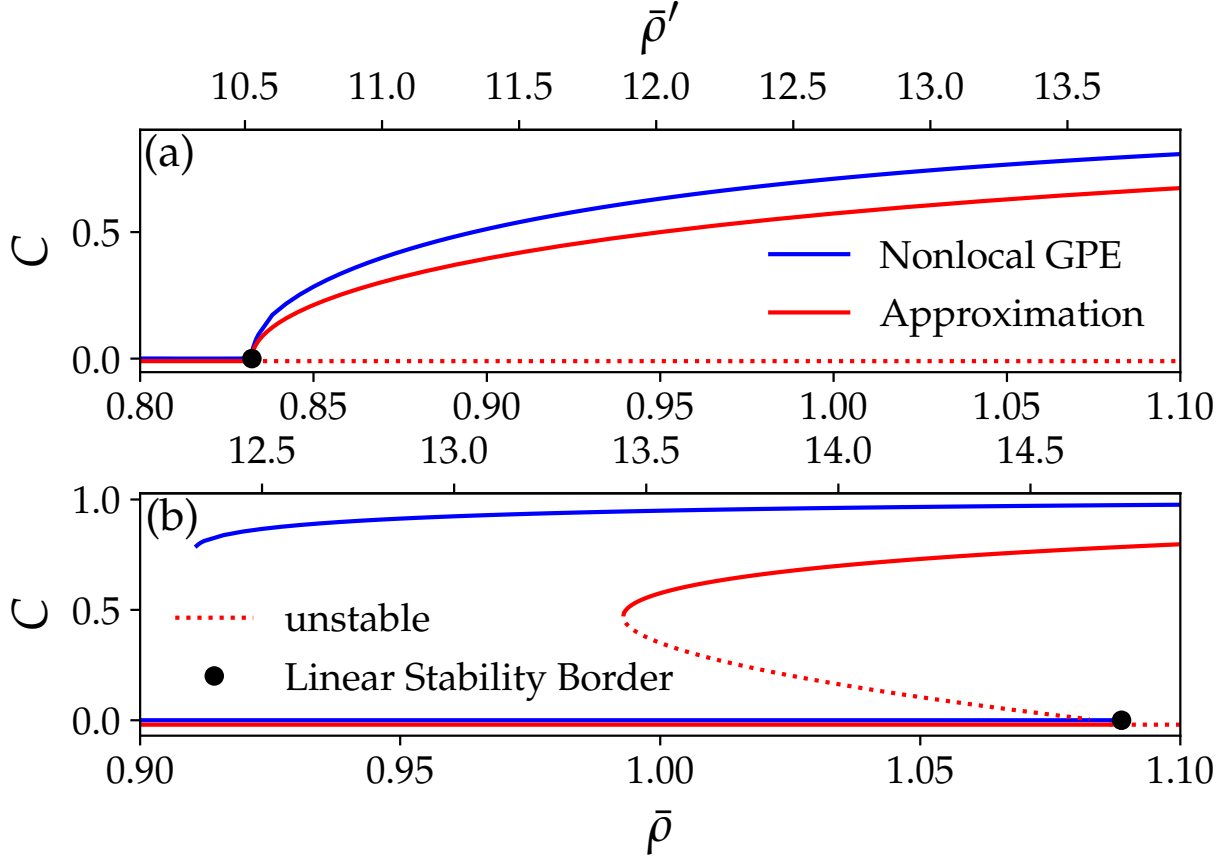


FIG. 2. Comparison between steady states of the GPE [Eq. (1), blue line] and its approximation [Eq. (17) or (9), red line]. The contrast C [Eq. (26)] is shown for (a) 1D and (b) 2D systems as a function of the mean density $\bar{\rho}$ and $\bar{\rho}'$. The domain size correspond to multiple of $2\pi/k_c$. The black filled circle indicates the linear stability threshold [cf. Fig. 1 (b-d)].

1. One-dimensional results

In one spatial dimension and with a cubic nonlinearity in Eqs. (1) and (9) the bifurcation between a uniform perfect superfluid and a modulated state is typically supercritical (see Appendix B) as illustrated in the corresponding example in Fig. 2(a).

In case of a transition between states in a system without mass conservation the terms “second order” and “supercritical bifurcation” are synonymous. However, there are systems with mass conservation that show supercritical bifurcations in a bifurcation diagram with mean density as control parameter, but still feature first order phase transitions and coexistence of states. This statement might seem contradictory, however, its validity rests in the fact that coexisting states

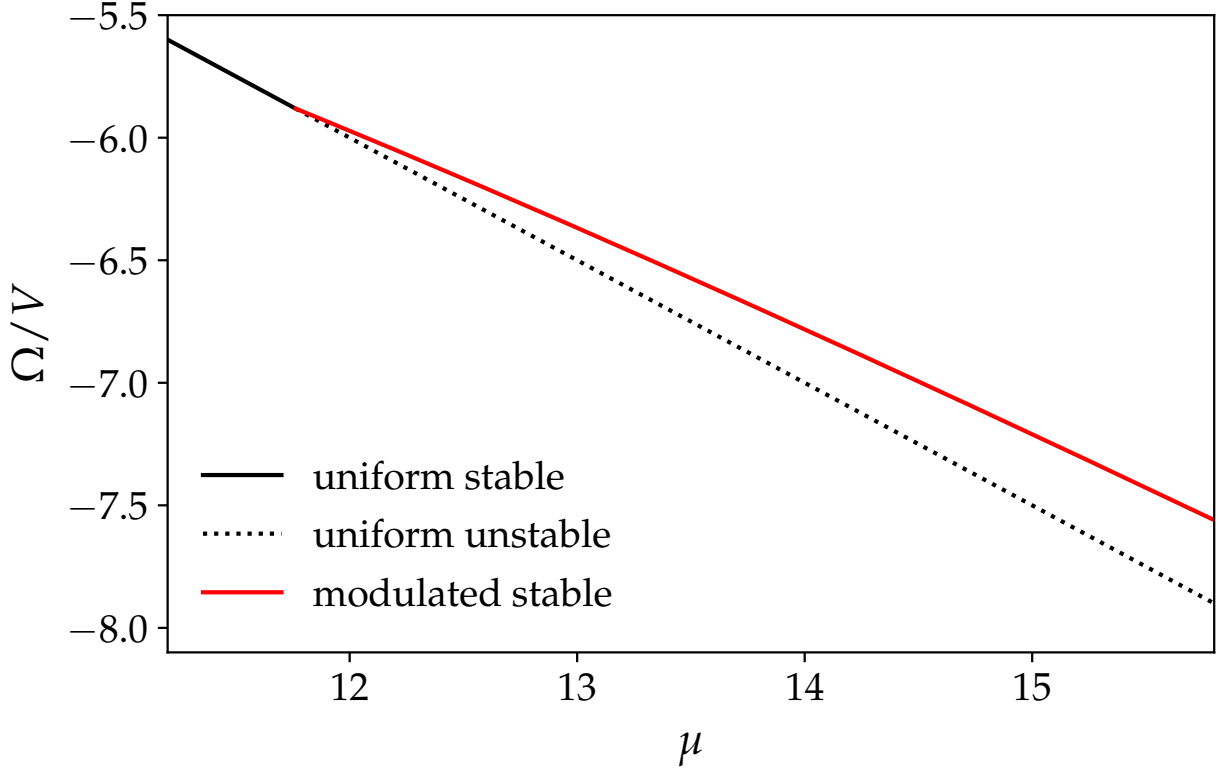


FIG. 3. The grand potential density Ω/V is given as a function of the chemical potential μ for the patterned and uniform states in the approximated 1D case of Fig. 2 (a). Modulated and uniform states are given as red and black lines, respectively. Solid and dashed lines refer to stable and unstable states, respectively. As the lines do not cross, uniform and modulated states do not coexist and no localized states exist.

normally represent different mean densities, i.e., are located at different values of the control parameter. A direct consequence of such coexisting states is the possible presence of localized states. Such a presence can then be taken as indicative for the existence of a first order transition. To assess this possibility, one has to check in detail whether states of identical chemical potential μ and grand potential Ω but different mean density exist. These are then the states coexisting in the thermodynamic limit. A well analyzed example is provided by the phase field crystal model.^{35,41,42}

To test this condition, we plot the grand potential density Ω/V as a function of the chemical potential μ for the branches of uniform and patterned states in Fig. 3 obtained with the approximated model presented in Fig. 2 (a). For the coexistence of the patterned and the uniform phase a crossing of the curves for two different stable states is required.⁴¹ As such a crossing does not occur, we conclude that in the considered parameter region, the transition is indeed of second order. This also implies that no localized states can be expected.⁵⁶

2. Results in Two Dimensions

To determine patterns in two dimensions and their ranges of stability as a function of $\bar{\rho}$, we use pseudo-arclength continuation at different fixed values of α_u . Thereby, the domain size is optimized for a hexagonal pattern with the critical wavenumber k_c . The corresponding length is $L_c = \frac{2\pi}{k_c}$ resulting in the domain size $L_x \times L_y = \frac{2}{\sqrt{3}}L_c \times 2L_c$. Note that periodic BC are required, in particular, to accurately predict the stability of the stripe phase and related secondary bifurcations. Neumann BC do not allow for certain changes of symmetry, resulting in missing unstable modes and therefore bifurcations.⁵⁷

Examples of the different occurring patterns are shown in Fig. 4. In particular, we present up-hexagons (hexagonal pattern of peaks Fig. 4 (a)), a honeycomb or down-hexagon pattern (hexagonal pattern of holes Fig. 4 (b)), stripe pattern (Fig. 4 (c)) and a rectangular pattern of peaks (Fig. 4 (d)). The latter is a consequence of the rectangular domain allowing for hexagons. On a square domain, these would become square patterns, but no ideal hexagonal patterns would exist.

Figure 5 presents the resulting bifurcation diagram in the $(\bar{\rho}, C)$ -plane obtained at $\alpha_u = -0.4$. The critical wave vector is $k_c = 0.88$ leading to $L_c = 7.14$. One can see that the uniform state undergoes a primary bifurcation at the expected critical value of $\bar{\rho}_c = 0.555$. At this transcritical bifurcation, coming from low densities, the stable uniform state loses stability and the unstable hexagon branch (blue line) at $\bar{\rho} < \bar{\rho}_c$ becomes the honeycomb branch (purple line) at $\bar{\rho} > \bar{\rho}_c$ that is also unstable. The hexagon branch passes a saddle-node bifurcation at $\bar{\rho} = 0.498$ (where it stays unstable, but with fewer unstable modes) and turns back towards larger mean densities. It stabilizes at a pitchfork bifurcation at $\bar{\rho} = 0.512$, i.e., below $\bar{\rho}_c$. This implies that there exists some hysteresis that in practice can lead to a jump in the amplitude typical for a first order phase transition.

In addition to the hexagon/honeycomb branches an unstable branch of stripe patterns (red line) also emerges at the primary bifurcation. When ignoring all other lines the bifurcation would be classified as a supercritical pitchfork. In the considered finite rectangular domain, the branch of rectangular patterns (orange line) emerges in a subcritical pitchfork bifurcation from the branch of stripes. Both are always unstable. Note that in an infinite system it would correspond to a branch of square patterns and also emerge from in the primary bifurcations.

As in the 1D case we test the stable states for thermodynamic coexistence by plotting in Fig. 6 the grand potential density Ω/V as a function of the chemical potential μ for the corresponding

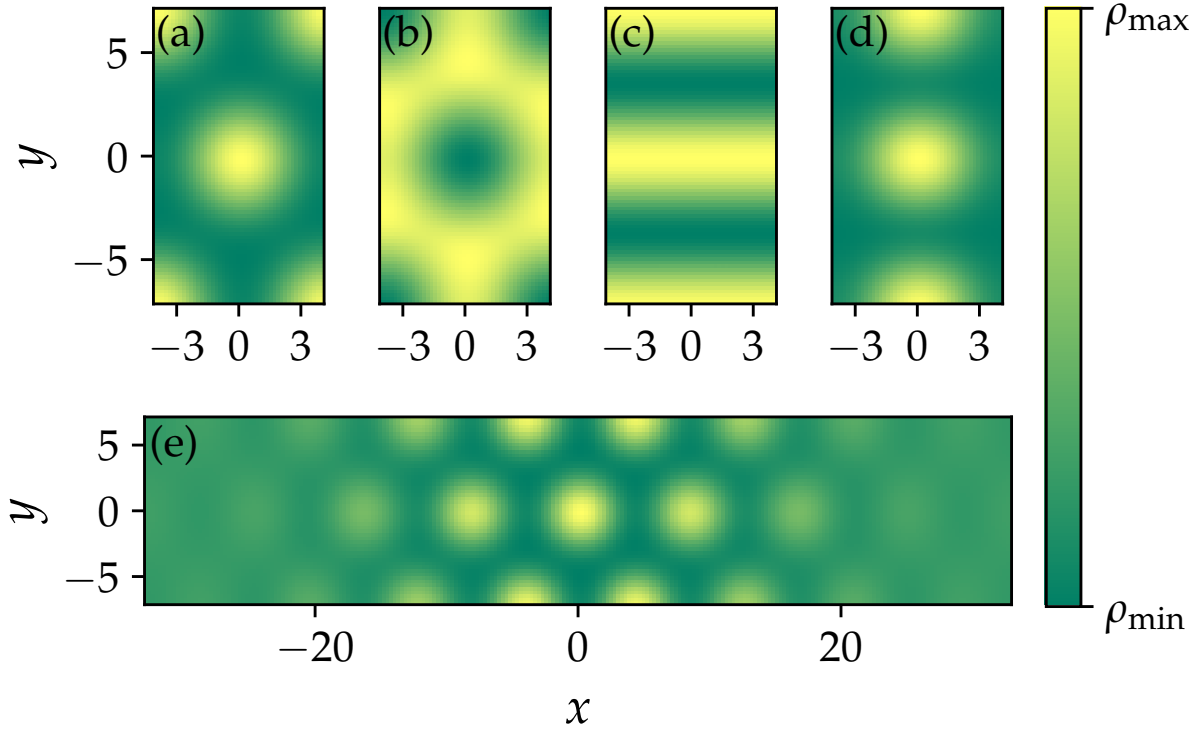


FIG. 4. Patterns occurring in a two-dimensional system at $\alpha_u = -0.4$: (a) hexagon, (b) honeycomb, (c) stripe (d) rectangle and (e) localized state corresponding to a patch of patterned state in background of uniform ground state. The domain sizes $L_x \times L_y$ are (a)-(d) $\frac{2}{\sqrt{3}}L_c \times 2L_c$ and (e) $16L_c/\sqrt{3} \times 2L_c$.

branches. Indeed this time, in contrast to the 1D result, the corresponding lines cross indicating that stable uniform state and stable hexagonal pattern can coexist in an infinite domain. Note that the corresponding states have different densities and are marked in the bifurcation diagram Fig. 5 by two filled blue circles. This indicates that at a sufficiently large domain size the system exhibits localized states, for instance, for a domain size $16L_c/\sqrt{3} \times 2L_c$ given by the gray line in Fig. 5. A corresponding profile is given in Fig. 4 (e). Note that this localized state is only localized in x -direction, while it is periodic in y -direction. In case of a small 2D system which cannot host localized states, the hexagons stabilize directly at their saddle-node bifurcation, while the jump to the hexagons as the energetically favored state occurs at $\bar{\rho} = 0.505$.

Coming back to the branch of localized states in Fig. 5 we notice that it does not seem to exhibit the expected typical snaking behaviour found, e.g., in the PFC model.⁴¹ This is also the case for larger domain sizes of up to $24L_c/\sqrt{3} \times 2L_c$ where one would usually find pronounced snaking behaviour (see, e.g., Ref. 58). However, Ref. 35 shows that in the PFC model a larger effective

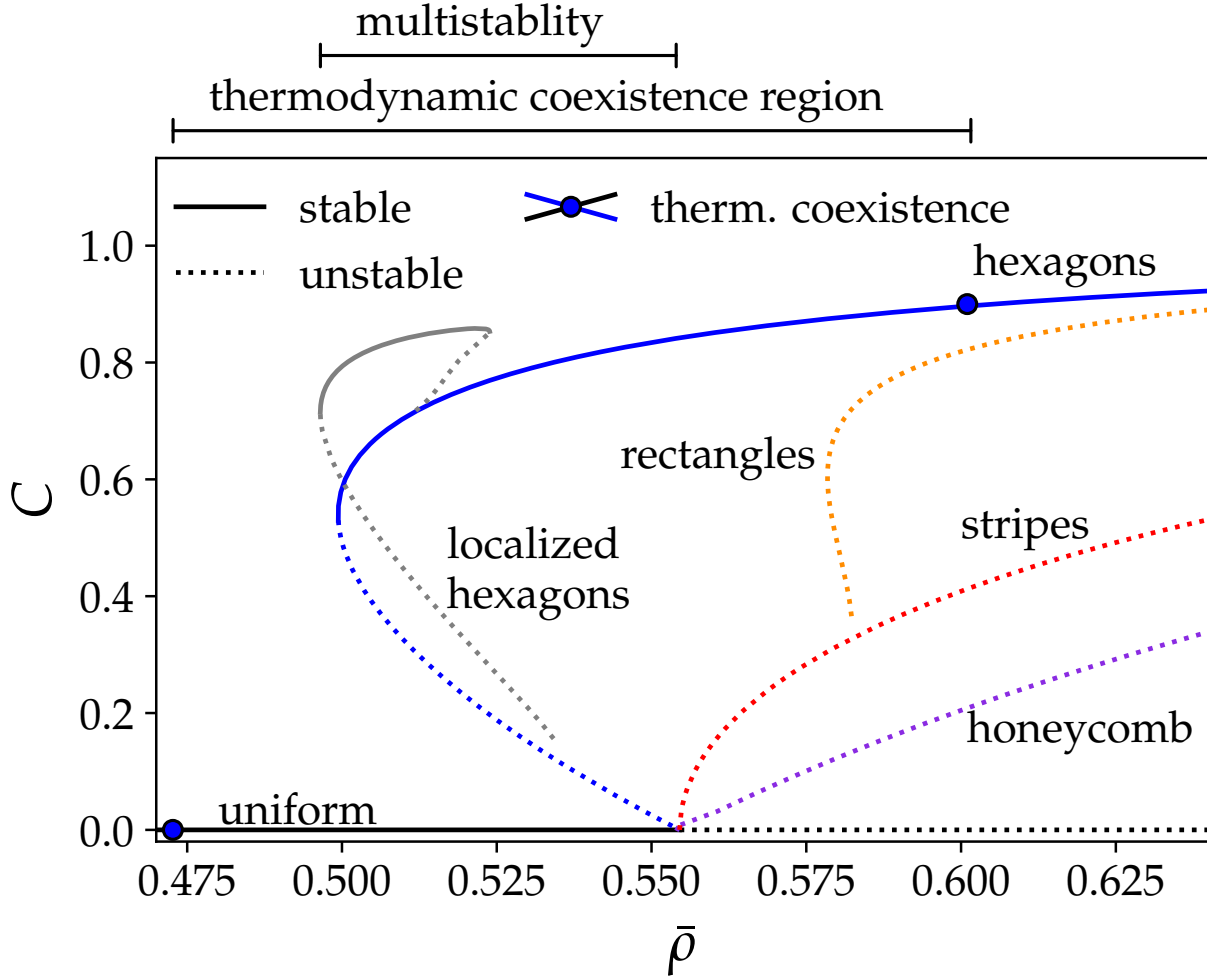


FIG. 5. Bifurcation diagram of the steady state solutions in 2D of Eq. 17 as a function of $\bar{\rho}$ at fixed $\alpha_u = -0.4$. The domain sizes are as in Fig. 4. The solutions are characterized through the contrast C [see Eq. (26)]. Solid and dotted lines represent stable and unstable states, respectively. The respective patterns are indicated at the curves. The two filled blue circles represent stable states coexisting in a infinite domain (identical grand potential and chemical potential (see Fig. 6). This indicates the range where localized states (grey line) may, in principle, exist.

temperature eventually destroys the pronounced snaking that involves saddle-node bifurcations of the branches of localized states. The number of peaks still changes when going along the branch, however, all saddle-node bifurcations have been annihilated. We believe that in the present case the value of α_u is too high for snaking to be found. Indeed, lowering α_u leads to steeper transitions between the uniform background and the patterned part within the localized states. However, as the system reacts very sensitively to a decrease in α_u , we are not able to lower it significantly

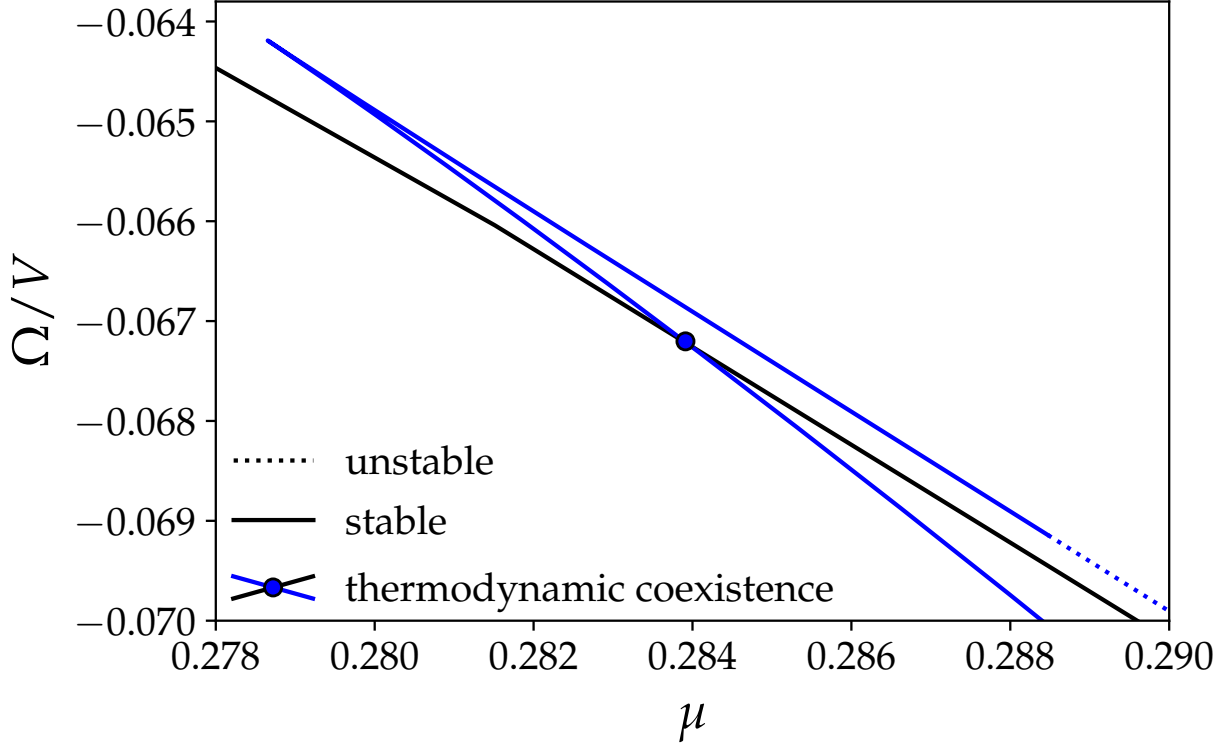


FIG. 6. The grand potential density Ω/V as a function of the chemical potential μ for the branches of hexagonal patterns (blue lines) and uniform states (black lines) is shown for the 2D case in Fig. 5. The crossing of the lines marked by a filled circle indicates that these states can coexist and localized states may exist. The coexisting states are also marked in Fig. 5.

further due to the occurrence of negative densities that result in a break down of the numerical procedure. Finally, the lack of a second branch of localized states with an even number of lines of peaks (cf. Fig. 15 (d) of Ref. 41) is due to the numerical limitation of the size of the box and the choice of Neumann BC [Fig. 4 (e)].

Further increasing the value of the interaction parameter to $\alpha_u = -0.216$ and $\alpha_u = -0.113$ results in the bifurcation diagrams shown in Figs. 7 (a) and 7 (b), respectively. First, inspecting Fig. 7 (a) and comparing it to Fig. 5 one notes that the branch of localized states does not exist anymore. In consequence, the hexagonal patterns become linearly stable directly at the saddle-node bifurcation. The bifurcation from the stripe state to the rectangles is replaced by a supercritical pitchfork bifurcation resulting in states that transform the stripes into an unstable superlattice-like pattern, namely, a rectangular arrangements of peaks with these rectangles being situated on a hexagonal lattice. This is allowed for by the Neumann BC applied to the same domain size as

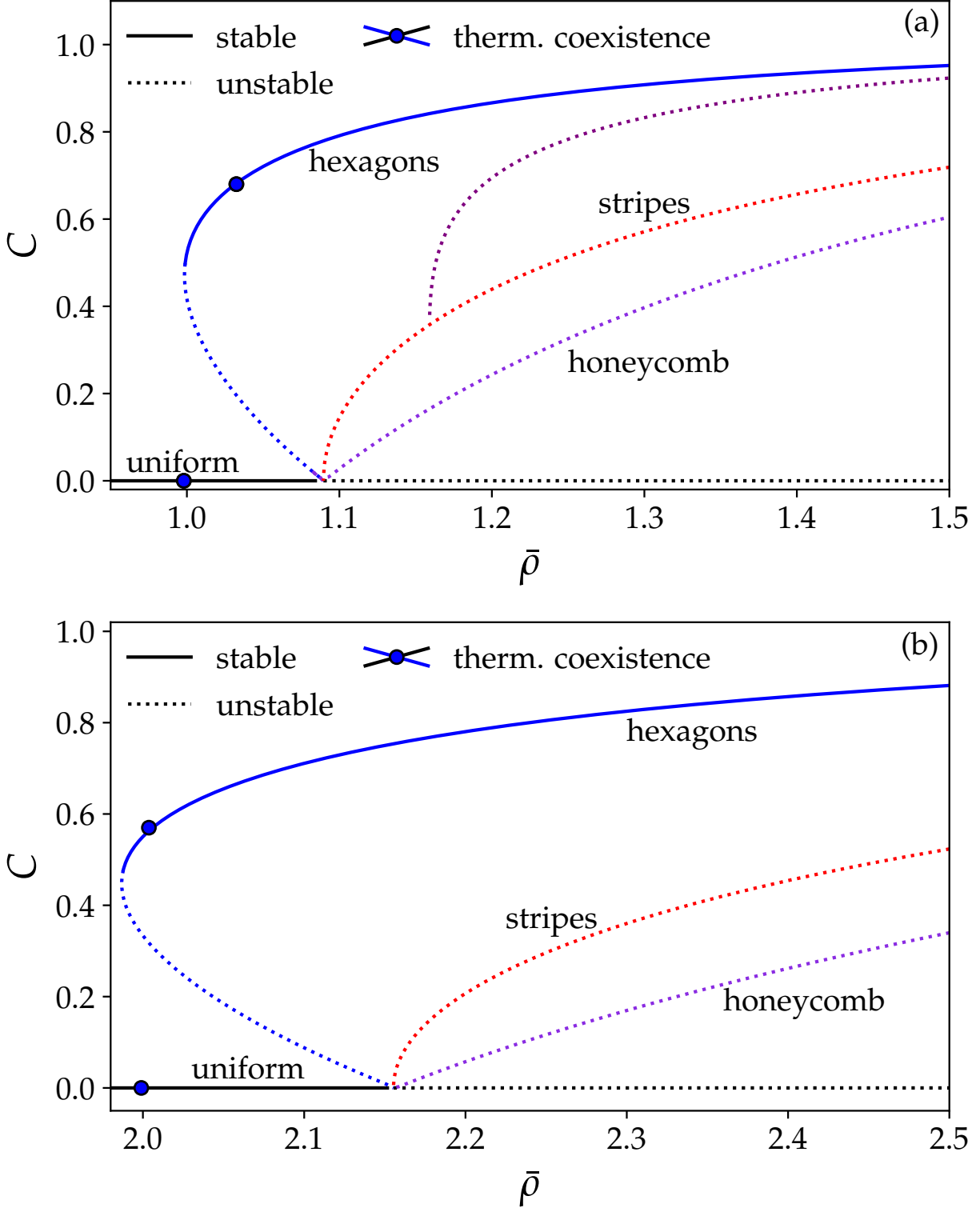


FIG. 7. Bifurcation diagrams of steady states of Eq. 17 in 2D as a function of $\bar{\rho}$ at fixed (a) $\alpha_u = -0.216$ and (b) $\alpha_u = -0.113$. The domain size is $2L_c/\sqrt{3} \times 2L_c$. Solution measure, line styles, markers and pattern types are as in Fig. 5. The purple line in (a) corresponds to a superlattice-like pattern, namely, a rectangular arrangement of peaks with these rectangles being located on a hexagonal lattice

before used with the periodic BC. This effectively corresponds to a doubled domain size with periodic BC.⁵⁹ The second length scale present in the superlattice pattern is not intrinsic to the model, but reflects the domain size. In other words, the confinement creates defects in the pattern that are then repeated periodically due to the boundary condition. The bifurcation's relative distance to the primary bifurcation is slightly larger than at $\alpha_u = -0.4$. Second, focusing on Fig. 7 (b), the picture has simplified as an increase in α_u rapidly moves the secondary bifurcation on the branch of stripes towards large densities outside the $\bar{\rho}$ -range of Fig. 7.

In both cases, the primary bifurcation occurs at the expected value, namely, at $\bar{\rho} = 1.09$ and $\bar{\rho} = 2.15$ in Fig. 7 (a) and (b), respectively. The saddle-node bifurcation on the branch of hexagonal patterns are at $\bar{\rho} = 1.99$ and $\bar{\rho} = 0.99$, respectively, i.e., with increasing $\bar{\rho}$ it moves further away from the primary bifurcation (in terms of relative density).

Summarizing, one may say that the range of bistability of hexagons and the uniform state increases with increasing interaction parameter α_u . However, in contrast to this the actual range of thermodynamic coexistence between the two states shrinks with increasing α_u as indicated by the decreasing density difference between the respective two filled circles in Figs. 5, 7 (a) and 7 (b) that indicate the coexisting states, i.e., the positions of the binodals. Also note that for the two larger α_u both respective binodal densities are in the density range where the uniform state is linearly stable. Thermodynamically speaking, the spinodal does not lie between the binodals. This is in contrast to PFC results^{35,41} and resembles the behaviour encountered in density functional theories of colloidal crystallization (cf. Fig. 2 of Ref. 60).

Even for a narrow coexistence region one would still expect localized states to exist. We believe that they could only be found for the parameters in Fig. 7(b) if a much larger domain size was used as at present possible for us. In accordance with Ref. 35 the increase in α_u leads to wider fronts between the pattern and the uniform state implying the need for larger domains.

IV. HIGHER-ORDER NONLINEARITIES

In the context of dipolar BECs it has been shown that deep quantum effects, so-called quantum fluctuations,⁶¹ can lead to qualitative changes in the stability properties of the accessible patterns.^{62–64} Furthermore, they can give rise to qualitative changes in the character of the phase transition: The hexagonal crystallisation into a supersolid can be of second order⁶² in contrast to the first order transition described above. Here, we qualitatively explore features facilitated by a

phenomenological addition of a higher-order nonlinearity to the equation of motion. This shall allow for an improved understanding of the emergence of the different phases and of accompanying changes in the bifurcation diagram. Note, however, that for illustration purposes the parameter values we consider are significantly larger than the values one would obtain in an actual computation of beyond mean-field corrections for the specific interaction considered here.

The considered nonlinearity has the form $|\Psi|^3\Psi$ with prefactor $b > 0$. Our (rescaled) governing equation (9) of motion is modified to

$$i\partial_t\Psi = \left(-\frac{\Delta}{2} + (\alpha_u + 1)|\Psi|^2 + 2\Delta|\Psi|^2 + \Delta^2|\Psi|^2 + b|\Psi|^3\right)\Psi. \quad (27)$$

The free energy functional defined by Eq. (22) as well as the steady state equation (13) are modified accordingly. We have

$$F = \int_V d^n r \left[\frac{|\nabla\rho|^2}{8\rho} + b\frac{2}{5}\rho^{5/2} + \frac{(\alpha_u + 1)}{2}\rho^2 + \rho\Delta\rho + \frac{\rho}{2}\Delta^2\rho \right] \quad (28)$$

and

$$\partial_t\rho = \Delta \left[\frac{(\nabla\rho)^2}{8\rho^2} - \frac{\Delta\rho}{4\rho} + (\alpha_u + 1)\rho + 2\Delta\rho + \Delta^2\rho + b\rho^{3/2} \right]. \quad (29)$$

In consequence, the equations (8) are no longer suitable and have to be adapted accordingly. This is done in Appendix A. Next, we investigate the changes caused by the unusual scaling of the additional nonlinearity.

A. Influence on Linear Stability

Inserting a uniform density with the perturbation $\rho - \bar{\rho} = \varepsilon \left(v e^{i(\omega t - \mathbf{kx})} - w e^{-i(\omega t - \mathbf{kx})} \right)$ into Eq. (29), where $\varepsilon \ll \bar{\rho}$, results in the amended dispersion relation

$$\omega'^2(k) = \omega^2 + \frac{k^2}{2} 3b\bar{\rho} \sqrt{\bar{\rho}}. \quad (30)$$

Perturbations grow exponentially when $\omega'^2 < 0$ with the threshold of instability at $\omega'^2 = 0$ which coincides with the emergence of nontrivial roots other than $k_0 = 0$:

$$k_0^2 = 1 - \frac{1}{8\bar{\rho}} \pm \sqrt{\left(1 - \frac{1}{8\bar{\rho}}\right)^2 - \left(\alpha_u + 1 + \frac{3}{2}b\sqrt{\bar{\rho}}\right)}. \quad (31)$$

Therefore in a system of infinite size the threshold of instability, where only one $k_0 = k_c$ exists, can be described through Eq. (32), where α_{uc} is the critical value of α_u . It is depicted in Fig. 8.

$$\alpha_{uc} = \left(1 - \frac{1}{8\bar{\rho}}\right)^2 - 1 - \frac{3}{2}b\sqrt{\bar{\rho}} \quad \text{for} \quad \bar{\rho} \geq \frac{1}{8}. \quad (32)$$

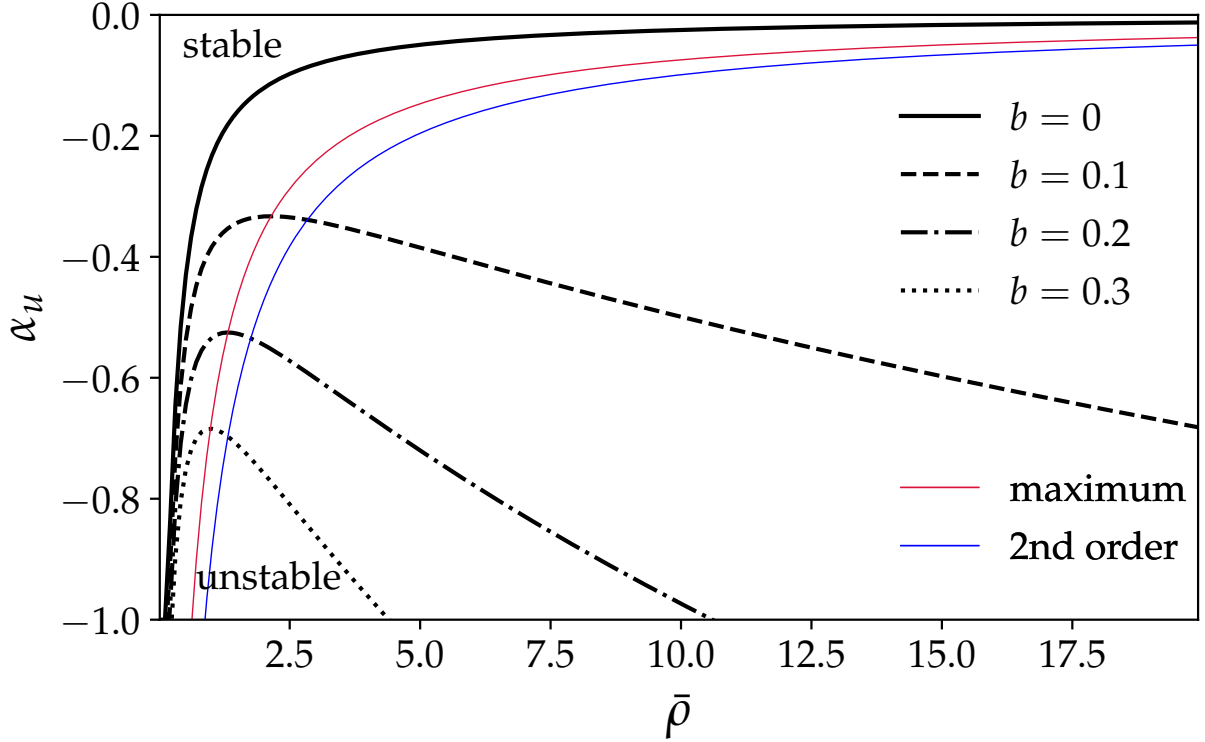


FIG. 8. Linear stability region of the uniform (superfluid) state $\rho(x) = \bar{\rho}$ in the $(\bar{\rho}, \alpha_u)$ plane. The stability thresholds according to Eq. (32) are given as black lines for various values of the strength of the quantum fluctuation term b . Thereby, the solid line corresponds to the case without the quantum fluctuation term, while the dashed, dot-dashed and dotted lines correspond to $b = 0.1$, $b = 0.2$ and $b = 0.3$, respectively. The regions above the respective lines correspond to stable uniform states. The thin red line indicates the position of the maximum of the curves when continuously changing b . Note that for $b \rightarrow 0$ the corresponding $\bar{\rho}$ also diverges. Correspondingly, the thin blue line indicates the position of the quadruple point where the phase transition is of second order (for details see main text). To the left [right] of the blue line the first stable pattern is the hexagon [honeycomb]. In both cases the phase transition is of first order.

As expected from the arguments laid out in Ref. 62, the higher-order (quartic) nonlinearity in Eq. (27) significantly changes the phase diagram. This is illustrated in Fig. 8 which shows the critical α_{uc} as a function of $\bar{\rho}$. At $b = 0$ we see that $\alpha_{uc}(\bar{\rho})$ has no local maximum, instead the maximum is at infinite $\bar{\rho}$. However, for nonzero values of b the maximum moves to finite values of $\bar{\rho}$ – its changing position is indicated by the red line. In consequence, for increasing b the region of stable uniform states is extended towards smaller values of α_{uc} and larger values of $\bar{\rho}$. The blue

curve indicates the single point at each value of b where the phase transition is of second order. As explained below, this is computed from a one-mode approximation. In other words, the line mark the parameter values where the transcritical bifurcation between uniform and hexagon/honeycomb pattern corresponds to orthogonally crossing branches, therefore giving no immediate hysteresis. In consequence, to the left of the blue line the first stable pattern is a hexagon (or possibly a localized hexagon state) while to the right it is a honeycomb (possibly localized).

B. Changes to Patterns and Phase Transition

To confirm the expected changes^{62–64} caused by the high-order nonlinearity in existence region and stability of different patterns and the corresponding phase transitions we apply a one-mode approximation (for details see Appendix B). In other words, the patterned state is approximated by harmonics of a single wavelength with small amplitude A . Inserting this ansatz into the free energy F combined with a Taylor expansion in $A \ll 1$ gives

$$F - F_0 = q_2 A^2 + q_3 A^3 + q_4 A^4 \quad (33)$$

which is a reasonable approximation close to the border of linear stability where the modulation amplitude A is small. Minimizing F with respect to k gives the critical wave number k_c and allows one to obtain the expressions for q_2 , q_3 and q_4 given in Table I in Appendix B. Minimizing F with respect to A one then determines the state of lowest energy.⁶²

As we only consider a polynomial in A up to fourth order, the results depicted in Fig. 9 only provide an approximate phase diagram. The expected hexagonal pattern forms the ground state in the low-density part of the region of linearly unstable uniform states. In contrast, in the high-density part the honeycomb pattern is of lowest energy while at intermediate densities the stripe phase dominates. Note that both, hexagon and honeycomb regions of dominance extend beyond the border of linear stability of the uniform state. This suggests a region of coexistence and therefore a first order phase transition. The coexistence region shrinks when approaching the quadruple point where the borders of thermodynamic stability meet for all four stable states. When crossing the phase boundary at this point there is no coexistence and therefore it corresponds to a second order phase transition.

The quadruple point is determined as an intersection of $q_3 = (16b\bar{\rho} - 8 + 1/\bar{\rho})3/256 = 0$ and Eq. (32). The latter relation characterizes the primary bifurcation and the former states that the

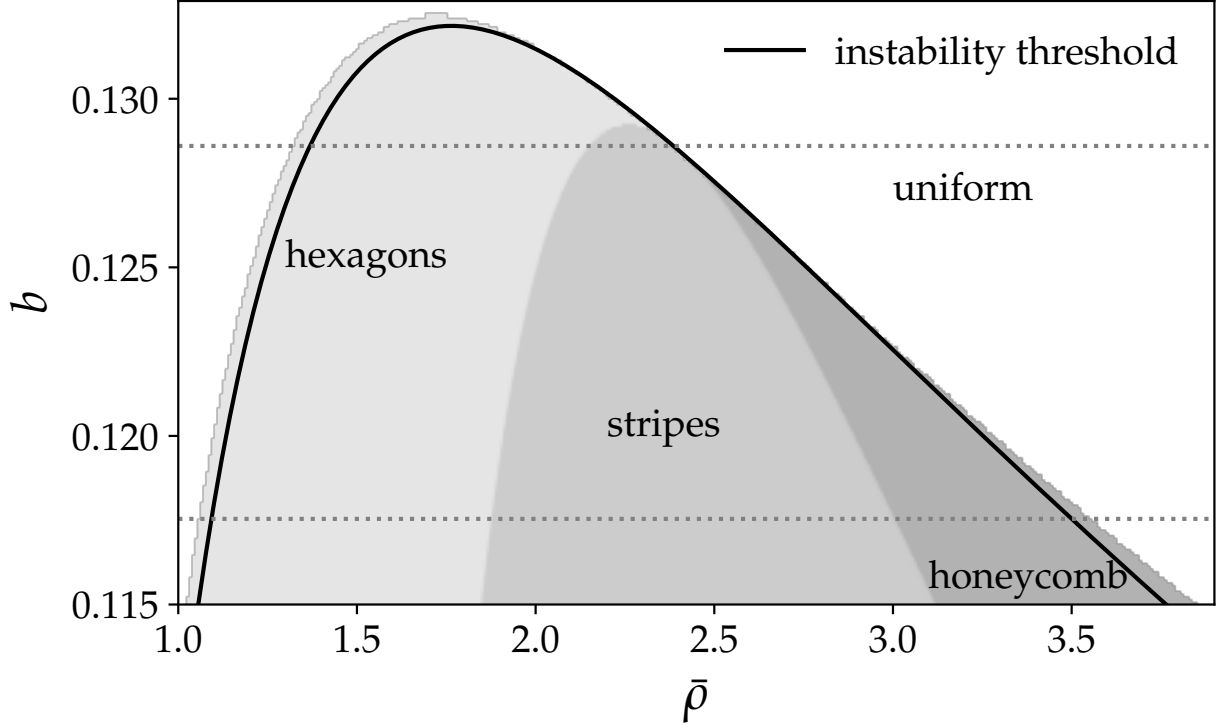


FIG. 9. Energetically favored ground states as obtained in a one-mode approximation at $\alpha_u = -0.4$. The border of stability, Eq. (32), is given as black line. The ground states are the uniform state (white region), hexagons (light gray region), stripes (medium gray region) and honeycomb (dark gray region). All four meet in a single point, where no coexistence with the uniform state exists, making it a second order phase transition. Horizontal dashed lines indicate b -values employed for the bifurcation diagrams in Figs. 11 and 12.

energy F only depends on even powers of the pattern amplitude, so neither hexagons (positive A) nor honeycombs (negative A) are favored. We find its location $(\alpha_{uQ}, \bar{\rho}_Q)$ as function of b or alternately $(b_Q, \bar{\rho}_Q)$ as function of α_u by solving

$$b_Q = \frac{8\bar{\rho} - 1}{16\bar{\rho}^{5/2}} \quad (34)$$

$$\alpha_{uQ} = \frac{7}{64\bar{\rho}^2} - \frac{1}{\bar{\rho}} \quad (35)$$

Alternatively, the blue line in Fig. 8 marks the resulting location of the quadruple point in the $(\bar{\rho}, \alpha_u)$ -plane for continuously changing b . Note that the quadruple point actually corresponds to a thermodynamic critical point. Its location within the phase diagram in Fig. 9 looks unusual because the parameters b , α_u and $\bar{\rho}$ are not independent.

The predicted existence of different phase transitions is highlighted in the corresponding bifurcation diagram with $\bar{\rho}$ as control parameter as given in Fig. 10. It shows the branches of the emerging states of a two-dimensional system with $\alpha_u = -0.4$ at $b = 0.1286$. The parameters are chosen in such a way that at lower $\bar{\rho}$ a first order phase transition between uniform state and hexagons is found while at higher $\bar{\rho}$ the quadruple point is passed, i.e., at this specific value of b , this bifurcation is of higher codimension and stable hexagons and stripes both emerge vertically. The domain size is again chosen to fit hexagonal states with $2L_c/\sqrt{3} \times 2L_c$.

At lower densities we see the expected transcritical bifurcation which here indicates a first order phase transition. Again, the filled circles indicate coexisting uniform and hexagon states, i.e., states of identical chemical potential and grand potential density. This implies that localized states could exist in principle, but are not observed at the domain sizes we are able to consider. At higher densities, however, the bifurcation occurs on the critical point, i.e., at the specific parameter value where the transcritical bifurcation between hexagons and honeycombs and the related saddle-node bifurcation of the hexagons exactly coincide. As there are no points of identical chemical potential and grand potential density, there are no points of coexistence of these states with the uniform state, and the corresponding phase transition is of second order. Note furthermore that the honeycomb state is unstable everywhere on the branch, while the stripe state has a narrow linearly stable region at high densities. However, in contrast to the result of the one-mode approximation (Fig. 9), it never becomes the energetically favored state, but only reaches the same low energy as the hexagons.

Figure 11 shows the bifurcation diagram of steady states at fixed $\alpha_u = -0.4$ and $b = 0.1286$ (along the upper horizontal line in Fig. 9). Then shadings highlight regions where the four different possible states are globally stable, i.e., correspond to the ground states. There are four transitions between them, for each we indicate respective pairs of coexisting states that have identical chemical potential and grand potential density and here show nearly the same value of $\bar{\rho}$ with the difference being of order 10^{-2} or lower. Again, in consequence of the coexisting states we expect localized states to exist that could be calculated in larger domains. The coexistences imply that all transitions are of first order. There are the first order phase transitions at low and high densities between the uniform state and hexagon and honeycomb patterns, respectively. Both are related to a combination of transcritical and saddle-node bifurcations. Furthermore, the $\bar{\rho}$ -range of globally stable stripe patterns ends at first order transitions to hexagons and honeycombs, respectively. Starting at low $\bar{\rho}$, the uniform state is energetically favoured up to $\bar{\rho} = 1.07$, followed by

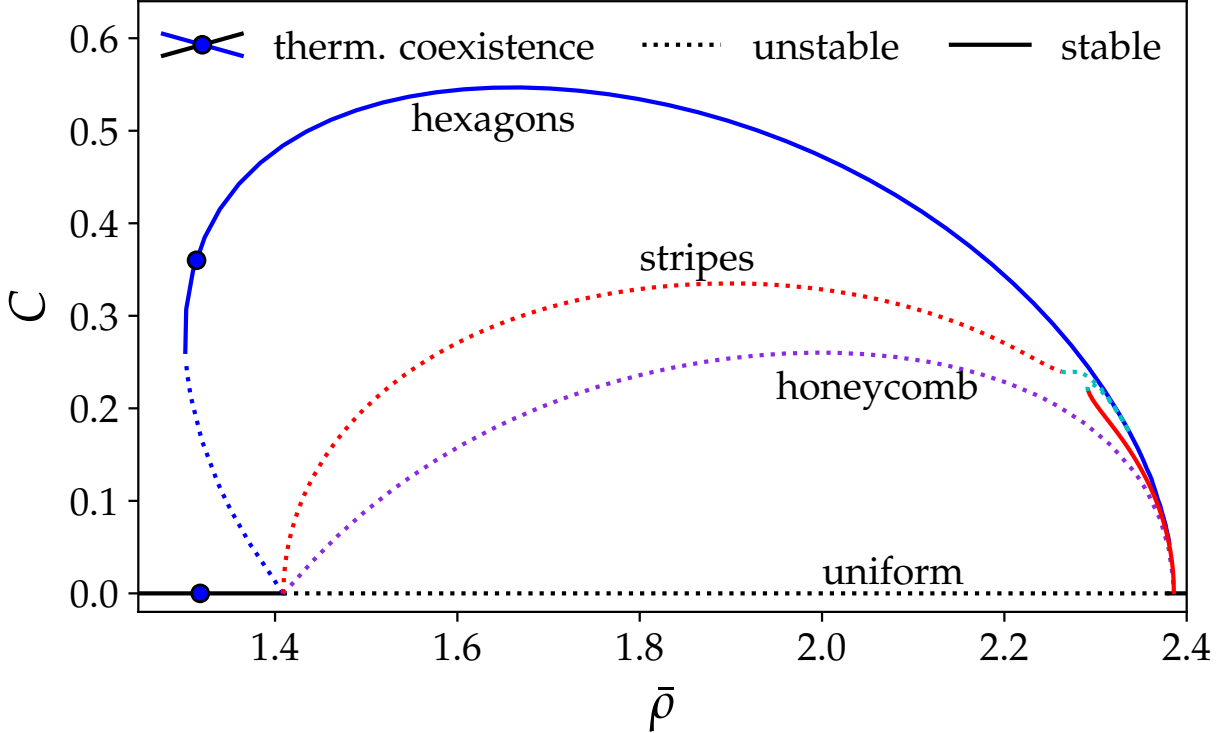


FIG. 10. Bifurcation diagram showing branches of steady states of Eq. (29) as a function of $\bar{\rho}$ at fixed $\alpha_u = -0.4$ and $b = 0.1286$ (along the upper horizontal line in Fig. 9). The considered 2D system has domain size $2L_c/\sqrt{3} \times 2L_c$. The solutions are characterized through the contrast C (see Eq. (26)). Line styles are as in Fig. 7 with the addition of stripe to hexagon transition states in cyan. The bifurcation at low $\bar{\rho}$ is related to points of thermodynamic coexistence between the uniform and hexagon states (indicated by filled circles). No such coexistence occurs for the bifurcation at high $\bar{\rho}$ that is related to a second order transition.

hexagons up to $\bar{\rho} = 2.7$. Then, stripes have the lowest energy until $\bar{\rho} = 3.28$ where honeycombs take over. Finally, at $\bar{\rho} = 3.56$ the uniform state becomes again dominant.

The line connecting stable and unstable hexagons [honeycombs] is interrupted by a small gap, as numerically the corresponding pitchfork bifurcations becomes a perturbed pitchfork because the numerical grid does not fully reflect the symmetries of the involved patterns. Typical profiles of state from the transition branch between stripes and hexagons/honeycombs are given in Fig. 12. The sequence starts with a stable hexagon pattern (leftmost image), transitions into stripes (central image), before becoming a honeycomb (rightmost image). Close inspection shows why it is necessary to use appropriate BC in the y -direction: while the hexagon-stripe transition works well

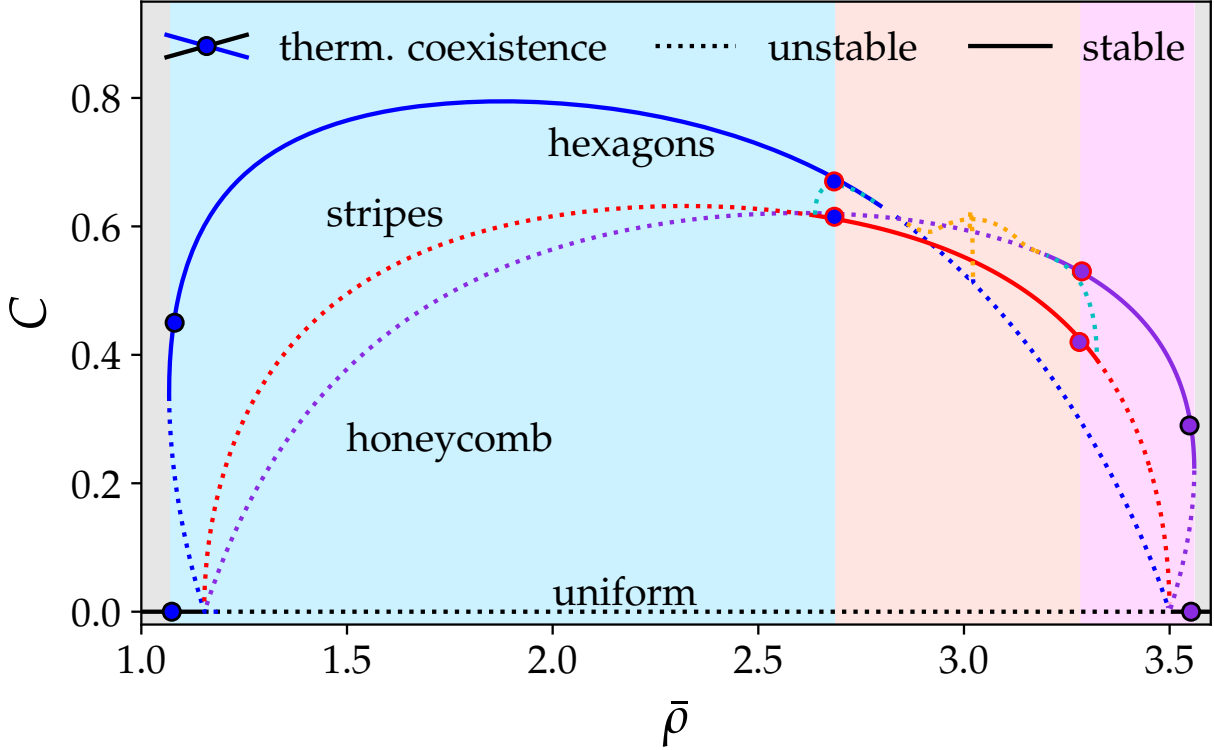


FIG. 11. Bifurcation diagram as in Fig. 10 at smaller $b = 0.1175$ (along the lower horizontal line in Fig. 9). Domain size, line styles, solution measure and markers are as in Fig. 10. The additional dotted orange lines correspond to transition states between hexagons and honeycombs. The background shading locally matches the colors of the respective ground state. Thermodynamic coexistence of pairs of states is marked by filled circles: the two colors of filling and contour refer to the respective coexisting states.

with Neumann BC, the subsequent stripe-honeycomb transition requires periodic BC. Note that the reverse is true when starting from a periodic honeycomb pattern that is placed in such a way in the finite domain that Neumann BC apply. This issue may lead to bifurcations of the plane filling patterns being missed when considering finite domains. In consequence it may even result in stripe patterns that are shifted by half a period showing different stabilities. Therefore, bifurcation diagrams for finite domains have to be carefully interpreted.

There exist further transition states on connecting branches between hexagon and honeycomb states (orange dotted lines in Fig. 11). These unstable patterns include triangles and patchwork quilt patterns (as in Ref. 65, chapter 5.4). We do not exclude the possibility of further connecting branches between these states, but expect all of them to be unstable. Note, however, that in consequence of the various unstable states time evolutions may show intricate behaviour in the

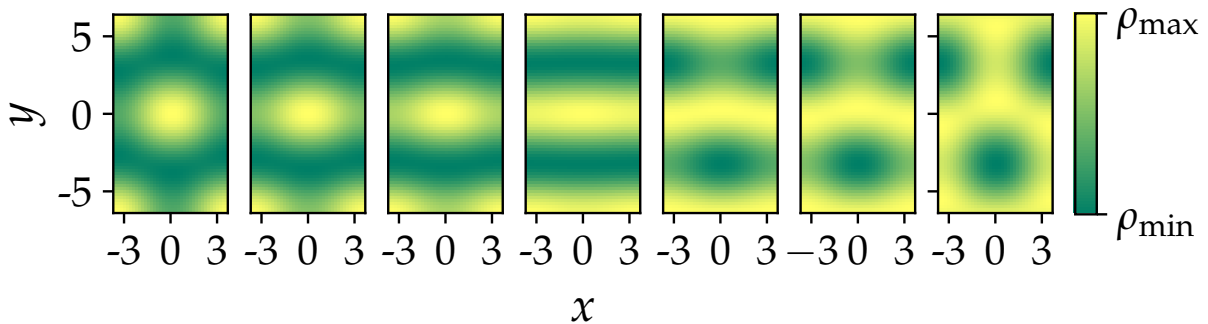


FIG. 12. Examples of steady patterns illustrating the transition from hexagons to stripes and further to honeycombs in Fig. 11 (for parameters see its caption). The sequence is as follows: From left to right there are a stable hexagon at $\bar{\rho} = 2.75$, unstable transition states at $\bar{\rho} = 2.7$ and $\bar{\rho} = 2.69$, a stable stripe at $\bar{\rho} = 2.67$, unstable transition states at $\bar{\rho} = 3.27$ and $\bar{\rho} = 3.25$, and a stable hexagon at $\bar{\rho} = 3.19$.

$\bar{\rho}$ -range around $\bar{\rho} = 3.0$ as unstable states may first attract and then repel the evolution, e.g., a time simulation started with perturbed triangle patterns, first approaches an unstable patchwork quilt pattern before converging to the globally stable stripe pattern (not shown).

V. SUMMARY & CONCLUSIONS

In the present work, we have investigated a PFC type model for BECs, employing arclength continuation techniques, stability analysis and one-mode approximations. The results have been presented in the form of bifurcation diagrams and phase diagrams. As a first step, we have approximated the nonlocal GPE around the phase transition by a PFC model. To do so we have proposed an alternative approach to Ref. 38 that aims at matching the dispersion relations at the onset of instability of the uniform state. The approach is general and does not depend on the specifics of the interatomic interactions (or nonlocal nonlinearity in case of optics), as long as the dispersion relation shows the expected maxon-roton form.

We have then benchmarked the validity of the PFC model as an approximation for the behavior of the full nonlocal GPE (Eq. (1)): The PFC model is able to correctly predict the onset of modulational stability and shows qualitative agreement with the GPE regarding the order of the phase transition. However, there is a clear quantitative disagreement between the models when comparing finite-amplitude modulated steady states. This can be expected as we only expanded to

fourth order.

Subsequently, we have presented bifurcation diagrams for spatially one and two dimensional systems, detailing possible steady states, coexistence regions and the existence of localized states. To the authors knowledge, localized states have not been discussed in depth in the context of BECs. Their analysis could turn out to be quite useful to experiments, as rich information could be extracted from individual images of a localized state.

As expected, in the analyzed case no localized states have been encountered in a one-dimensional system with cubic nonlinearity.⁶⁶ However, we have found localized states in the two-dimensional system. Although they were found employing an approximative local model, we conjecture that these states also persist in the full nonlocal model. Here, it has turned out to be numerically convenient to choose sufficiently low values of the interaction parameter α_u , as this leads to smaller transition regions between coexisting states. Nonetheless, we have to caution that the model is not suitable for excessively low values of α_u , which result in unphysical negative densities. Note that we did not encounter slanted snaking of branches of localized states, which could have been expected in analogy to similar systems.³⁵ Most likely this is due to computational limitations that do not allow us to consider very large domains at interaction parameters sufficiently far from the critical point.

In the final part we have considered how a phenomenological addition of a higher-order nonlinearity (in analogy to quantum fluctuations in dipolar BECs) changes the structure of the bifurcation diagram. We have found that such a nonlinearity stabilizes superfluid states with high densities and adds additional stable patterns. This is in close similarity to what has been recognized in dipolar BECs,⁶²⁻⁶⁴ thereby underpinning that, despite of our dramatically different model, the general behavior and topology persist.

In summary, we have presented an approximate mapping that permits to employ standard bifurcation software and subsequently investigated bifurcation diagrams that include unstable states. In this way we have gained a deeper understanding of the specifics of the bifurcations present in the system. We believe that our results will remain qualitatively valid for other nonlocal GPE models and provide a reference case for their future bifurcation analysis. Note that the presented methods can also be applied to nonlocal optical systems that display pattern formation.^{36,37} Furthermore, the mapping could turn out to be useful for fast calculations of approximate excitation spectra as the matrix occurring in the Bogoliubov-de-Gennes equations that needs to be diagonalized is no longer full.^{21,28}

ACKNOWLEDGMENTS

Discussions with Max Holl and Tobias Frohoff-Hülsmann are acknowledged. F.M. acknowledges stimulating discussions with Yongchang Zhang and Thomas Pohl.

DATA AVAILABILITY STATEMENT

The data that support the findings of this study are openly available on zenodo at <http://doi.org/10.5281/zenodo.6594198>, in Ref. 67.

Appendix A: Deriving the Approximation Parameters with Higher Nonlinearities

Starting from the dispersion relation in Eq. (30), we once again replace $\hat{R}(k)$ with the polynomial in Eq. (3) and demand that the requirements from Eqs. (5)-(7) hold.

Given the critical values k_c and $\bar{\rho}_c$ of k and $\bar{\rho}$ we can now determine g_0 , g_2 and g_4 :

$$g_0 = \frac{2\hat{R}(k_c) + 4k_c\partial_k\hat{R}(k_c) + k_c^2\partial_{kk}\hat{R}(k_c)}{8} + \frac{3k_c^2}{8\bar{\rho}_c} - \frac{27b\sqrt{\bar{\rho}}}{8}, \quad (\text{A1})$$

$$g_2 = -\frac{1}{k_c^2} \left(2g_0 + \frac{k_c^2}{4\bar{\rho}_c} + \frac{3}{2}b\sqrt{\bar{\rho}} \right), \quad (\text{A2})$$

$$g_4 = \frac{1}{k_c^4} \left(g_0 + \frac{3}{2}b\sqrt{\bar{\rho}} \right). \quad (\text{A3})$$

$\partial_k\hat{R}$ and $\partial_{kk}\hat{R}$ are the first and second derivatives of \hat{R} with respect to k .

Those g_0 , g_2 and g_4 can now be used in the rescaling as before, with the addition of:

$$b \rightarrow b' \frac{\alpha_u + 1}{g_0} \sqrt{\frac{2}{-g_2}}. \quad (\text{A4})$$

Appendix B: One-Mode Approximation

The one-mode approximation is used to get the minimum energy by inserting the ansatz

$$\rho = \bar{\rho} + \bar{\rho}A \sum_{i=1}^3 \cos(\mathbf{k}_i \mathbf{r}) \quad (\text{B1})$$

for hexagons [honeycomb] with $A > 0$ [$A < 0$] or

$$\rho = \bar{\rho} + \bar{\rho}A \cos(\mathbf{k}_1 \mathbf{r}) \quad (\text{B2})$$

	hexagons/honeycomb	1D/stripes
q_2	$\frac{192\alpha_u\bar{\rho}^2+48\bar{\rho}+288b\sqrt{\bar{\rho}^5}-3}{256}$	$\frac{64\alpha_u\bar{\rho}^2+16\bar{\rho}+96b\sqrt{\bar{\rho}^5}-1}{256}$
q_3	$\frac{-24\bar{\rho}+48b\sqrt{\bar{\rho}^5}+3}{256}$	0
q_4	$\frac{240\bar{\rho}-90b\sqrt{\bar{\rho}^5}-33}{1024}$	$\frac{8\bar{\rho}-3b\sqrt{\bar{\rho}^5}-1}{512}$

TABLE I. Prefactors to the amplitudes in the energy equation (Eq. (B3)) of the one mode approximation up to fourth order, depending only on the model parameters.

for one dimensional solutions or stripes in two dimensions, into the energy F given by Eq. (28). The lattice vectors \mathbf{k}_i are $\mathbf{k}_1 = (k, 0)$, $\mathbf{k}_2 = (-k/2, k\sqrt{3}/2)$ and $\mathbf{k}_3 = (-k/2, -k\sqrt{3}/2)$. The amplitude of the pattern is $\bar{\rho}A$ and $A \ll 1$.

We get results of the form

$$F - F_0 = q_2A^2 + q_3A^3 + q_4A^4, \quad (\text{B3})$$

where F_0 is the uniform ground state energy at $A = 0$.

From there the energy is minimized first with respect to k , therefore $\partial_k F = 0$ at $k = k_c$. Inserting k_c into F and neglecting all terms of order $O(A^5)$ and higher gives the results in Tab. I.

In one dimension the sign of q_4 distinguishes between super- ($q_4 > 0$) and subcritical ($q_4 < 0$) pitchfork bifurcation. At $b = 0$ we get $q_4 > 0$ for $\bar{\rho} > 0.125$ meaning the bifurcation is supercritical as seen in the examples above. A subcritical pitchfork is not possible as $\bar{\rho} < 0.125$ and therefore $\alpha_u < -1$ is not a valid parameter region in this model.

For $b \neq 0$ we set b so it matches the border of linear stability (see Eq. (8)) where the bifurcation emerges and get $q_4 = \frac{64\alpha_u\bar{\rho}^2 + 272\bar{\rho} - 33}{16384}$, meaning

$$\frac{33}{64\bar{\rho}^2} - \frac{17}{4\bar{\rho}} \begin{cases} < \alpha_u \rightarrow \text{supercritical,} \\ > \alpha_u \rightarrow \text{subcritical.} \end{cases} \quad (\text{B4})$$

The former is always true for $0.125 < \bar{\rho} < 4.125$ as the model requires $\alpha_u > -1$. Beyond that subcritical bifurcations are possible.

Appendix C: Bifurcations in 1D

The patterns a one dimensional system of size $L = 20$ exhibits while keeping the mean density at a constant value of $\bar{\rho} = 1$ and varying α_u are depicted in the bifurcation diagram in Fig. 13, detailing which patterns appear at which values of α_u categorized by their mode and contrast C .

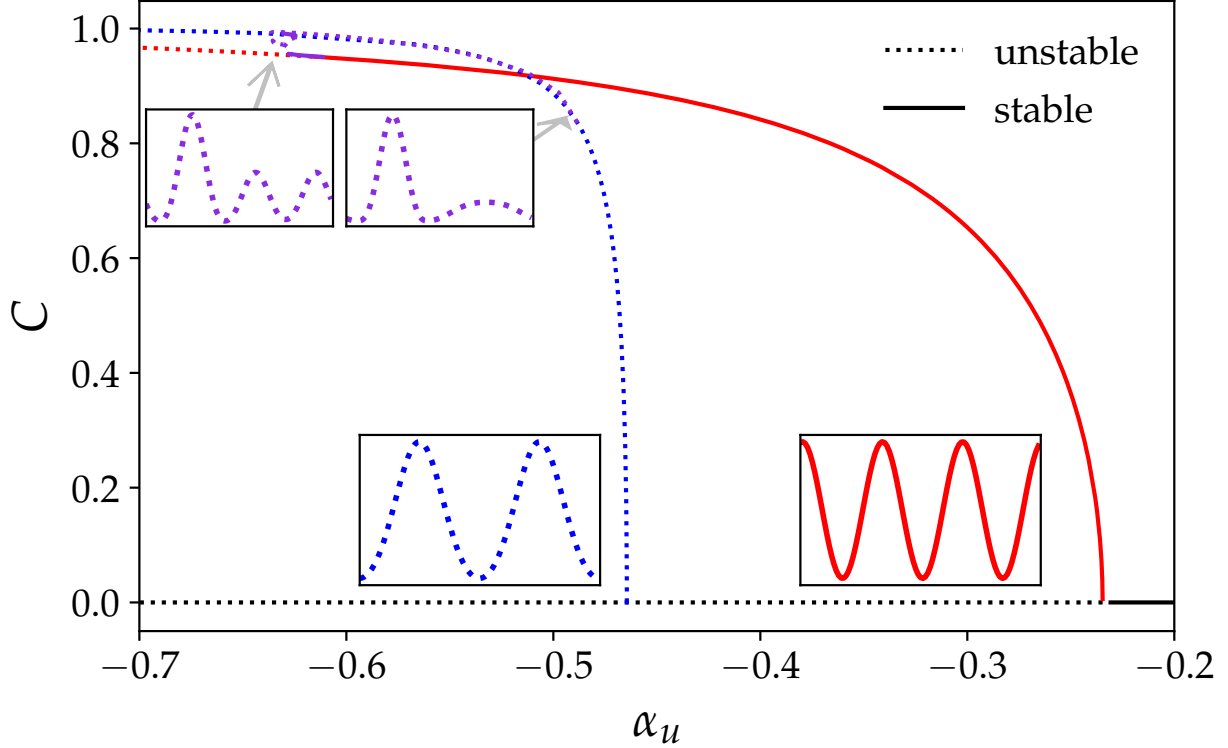


FIG. 13. Shown are branches of steady states of Eq. 17 as a function of the interaction parameter α_u at fixed $\bar{\rho} = 1$ and domain size $L = 20$. The states are characterized by their contrast C . Continuous and dotted lines represent stable and unstable states, respectively. The horizontal black line corresponds to the uniform state. The colored lines correspond to periodic states, where the red state has 3 peaks, the blue state has two peaks and the purple state has two peaks of alternating height, where the smaller peak eventually splits into two peaks of equal height. The phase transition between the uniform and patterned stable states is of second order and there are no localized states.

There is a phase transition between the uniform and the patterned state at $\alpha_u = -0.235$, matching the theoretical value for a system of size L with a mode number three. As the bifurcation is supercritical there is no hysteresis and therefore no jump in the amplitude, making this a second order phase transition. The mode three state is stable until around $\alpha_u = -0.62$, where the approximation reaches its limit, leading to states with negative densities and therefore no more stable states.

At finite system size of $L = 20$ there exists a second patterned state with mode number two, also emerging supercritical but unlike the mode three state it is unstable for all values of α_u .

There are also mixed states, where the system changes between the two modes, also unstable,

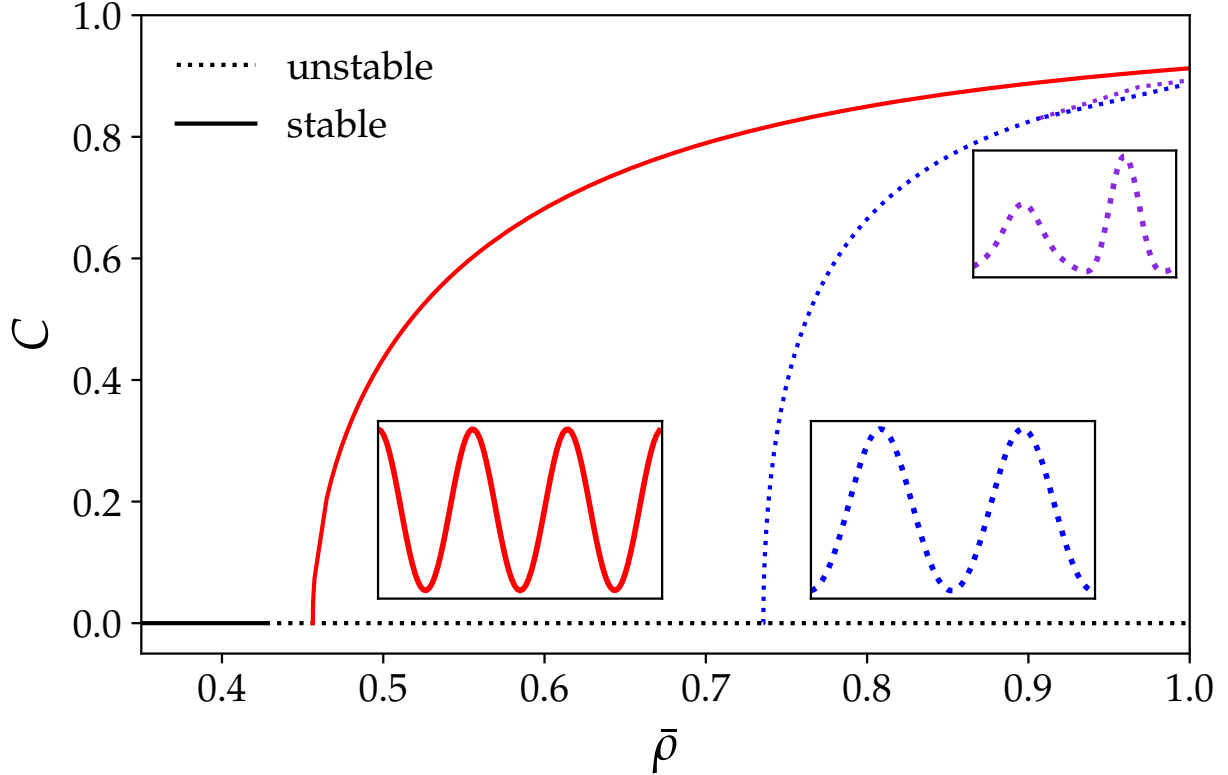


FIG. 14. Steady states of Eq. 17 as a function of $\bar{\rho}$ at fixed $\alpha_u = -0.5$ with the domain size $L = 20$. The solutions are characterized through the contrast C . Line styles are as in Fig. 13.

except for right at the border where the approximation is no longer usable, making their usefulness in predicting real systems somewhat sketchy.

The small gap between the end of the stable region for the uniform state and the onset of the stable patterned state is due to the threshold of instability matching the theoretical value for an infinite system, while the position of the bifurcation is influenced by the domain size.

Similarly a bifurcation diagram in a system of size $L = 20$ where $\bar{\rho}$ is varied while the interaction potential is kept at a specific form, represented by $\alpha_u = -0.5$, can be found in Fig. 14.

We find very similar results to those discussed for Fig 13, with supercritical bifurcations and second order phase transitions. Its position matches the theoretical value of $\bar{\rho} = 0.456$ for a system of size $L = 20$ and mode number 3.

As before we test for localized states by looking for states with equal chemical potential μ and grand potential density Ω , with the results shown in Figs. 15 (a) and (b), where we plotted the grand potential density $\omega = \Omega/L$ plotted against the chemical potential for the stable states of

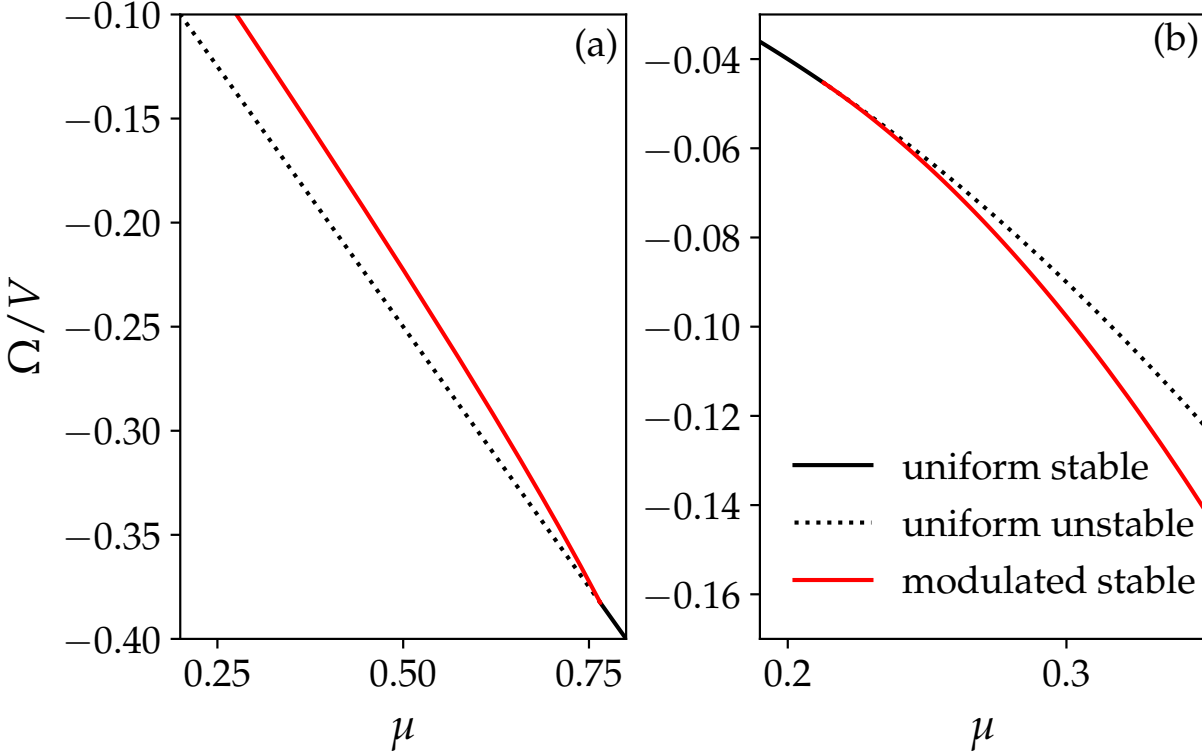


FIG. 15. Diagram of the grand potential density as a function of the chemical potential for the stable states in (a) Fig. 13 and (b) Fig. 14 with line styles matching those in Fig. 13. There are no cross sections and therefore no states which can coexist indefinitely.

Fig. 13 and 14 respectively.

As expected there is no crossing of the curves for two different stable states and therefore no localized states can be found.

REFERENCES

- ¹L. M. Pismen, *Patterns and Interfaces in Dissipative Dynamics*, 1st ed. (Springer Berlin Heidelberg, Berlin, Heidelberg, 2006).
- ²M. C. Cross and P. C. Hohenberg, “Pattern formation outside of equilibrium,” *Rev. Mod. Phys.* **65**, 851–1112 (1993).
- ³P. Ball, “In retrospect: On the six-cornered snowflake,” *Nature* **480**, 455–455 (2011).
- ⁴A. M. Turing, “The chemical basis of morphogenesis,” *Philos. Trans. R. Soc. Lond. Ser. B-Biol. Sci.* **23**, 237 (1952).

- ⁵J. Swift and P. C. Hohenberg, “Hydrodynamic fluctuations at the convective instability,” *Phys. Rev. A* **15**, 319–328 (1977).
- ⁶M. Hilali, G. Dewel, and P. Borckmans, “Subharmonic and strong resonances through coupling with a zero mode,” *Phys. Lett. A* **217**, 263 – 268 (1996).
- ⁷R. Lefever, N. Barbier, P. Couteron, and O. Lejeune, “Deeply gapped vegetation patterns: On crown/root allometry, criticality and desertification,” *J. Theor. Biol.* **261**, 194–209 (2009).
- ⁸M. Tlidi, P. Mandel, and R. Lefever, “Localized structures and localized patterns in optical bistability,” *Phys. Rev. Lett.* **73**, 640–643 (1994).
- ⁹N. Stoop, R. Lagrange, D. Terwagne, P. Reis, and J. Dunkel, “Curvature-induced symmetry breaking determines elastic surface patterns,” *Nat. Mater* **14**, 337–342 (2015).
- ¹⁰A. F. Andreev and I. M. Lifshitz, “Quantum theory of defects in crystals,” *Sov. Phys. JETP* **29**, 1107–1113 (1969).
- ¹¹A. J. Leggett, “Can a solid be “superfluid”?” *Phys. Rev. Lett.* **25**, 1543–1546 (1970).
- ¹²G. V. Chester, “Speculations on Bose-Einstein condensation and quantum crystals,” *Phys. Rev. A* **2**, 256–258 (1970).
- ¹³H. Kadau, M. Schmitt, M. Wenzel, C. Wink, T. Maier, I. Ferrier-Barbut, and T. Pfau, “Observing the Rosensweig instability of a quantum ferrofluid,” *Nature* **530**, 194–197 (2016).
- ¹⁴M. Schmitt, M. Wenzel, F. Böttcher, I. Ferrier-Barbut, and T. Pfau, “Self-bound droplets of a dilute magnetic quantum liquid,” *Nature* **539**, 259–262 (2016).
- ¹⁵D. S. Petrov, “Quantum mechanical stabilization of a collapsing Bose-Bose mixture,” *Phys. Rev. Lett.* **115**, 155302 (2015).
- ¹⁶C. R. Cabrera, L. Tanzi, J. Sanz, B. Naylor, P. Thomas, P. Cheiney, and L. Tarruell, “Quantum liquid droplets in a mixture of Bose-Einstein condensates,” *Science* **359**, 301–304 (2018).
- ¹⁷L. Tanzi, E. Lucioni, F. Famà, J. Catani, A. Fioretti, C. Gabbanini, R. N. Bisset, L. Santos, and G. Modugno, “Observation of a dipolar quantum gas with metastable supersolid properties,” *Phys. Rev. Lett.* **122**, 130405 (2019).
- ¹⁸F. Böttcher, J.-N. Schmidt, M. Wenzel, J. Hertkorn, M. Guo, T. Langen, and T. Pfau, “Transient supersolid properties in an array of dipolar quantum droplets,” *Phys. Rev. X* **9**, 011051 (2019).
- ¹⁹L. Chomaz, D. Petter, P. Ilzhöfer, G. Natale, A. Trautmann, C. Politi, G. Durastante, R. M. W. van Bijnen, A. Patscheider, M. Sohmen, M. J. Mark, and F. Ferlaino, “Long-lived and transient supersolid behaviors in dipolar quantum gases,” *Phys. Rev. X* **9**, 021012 (2019).
- ²⁰L. Tanzi, S. M. Roccuzzo, E. Lucioni, F. Famà, A. Fioretti, C. Gabbanini, G. Modugno, A. Re-

- cati, and S. Stringari, “Supersolid symmetry breaking from compressional oscillations in a dipolar quantum gas,” *Nature* **574**, 382–385 (2019).
- ²¹M. Guo, F. Böttcher, J. Hertkorn, J.-N. Schmidt, M. Wenzel, H. P. Büchler, T. Langen, and T. Pfau, “The low-energy Goldstone mode in a trapped dipolar supersolid,” *Nature* **574**, 386–389 (2019).
- ²²G. Natale, R. M. W. van Bijnen, A. Patscheider, D. Petter, M. J. Mark, L. Chomaz, and F. Ferlaino, “Excitation spectrum of a trapped dipolar supersolid and its experimental evidence,” *Phys. Rev. Lett.* **123**, 050402 (2019).
- ²³M. A. Norcia, C. Politi, L. Klaus, E. Poli, M. Sohmen, M. J. Mark, R. N. Bisset, L. Santos, and F. Ferlaino, “Two-dimensional supersolidity in a dipolar quantum gas,” *Nature* **596**, 357–361 (2021).
- ²⁴L. Tanzi, J. G. Maloberti, G. Biagioni, A. Fioretti, C. Gabbanini, and G. Modugno, “Evidence of superfluidity in a dipolar supersolid from nonclassical rotational inertia,” *Science* **371**, 1162–1165 (2021).
- ²⁵N. Henkel, R. Nath, and T. Pohl, “Three-dimensional roton excitations and supersolid formation in Rydberg-excited Bose-Einstein condensates,” *Phys. Rev. Lett.* **104**, 195302 (2010).
- ²⁶F. Cinti, P. Jain, M. Boninsegni, A. Micheli, P. Zoller, and G. Pupillo, “Supersolid droplet crystal in a dipole-blockaded gas,” *Phys. Rev. Lett.* **105**, 135301 (2010).
- ²⁷S. Saccani, S. Moroni, and M. Boninsegni, “Excitation spectrum of a supersolid,” *Phys. Rev. Lett.* **108**, 175301 (2012).
- ²⁸T. Macrì, F. Maucher, F. Cinti, and T. Pohl, “Elementary excitations of ultracold soft-core bosons across the superfluid-supersolid phase transition,” *Phys. Rev. A* **87**, 061602 (2013).
- ²⁹T. Macrì, S. Saccani, and F. Cinti, “Ground state and excitation properties of soft-core bosons,” *J. Low Temp. Phys.* **177**, 59 (2014).
- ³⁰F. Cinti, M. Boninsegni, and T. Pohl, “Exchange-induced crystallization of soft-core bosons,” *New J. Phys.* **16**, 033038 (2014).
- ³¹F. Maucher, N. Henkel, M. Saffman, W. Królikowski, S. Skupin, and T. Pohl, “Rydberg-induced solitons: Three-dimensional self-trapping of matter waves,” *Phys. Rev. Lett.* **106**, 170401 (2011).
- ³²M. D. Lukin, M. Fleischhauer, R. Cote, L. M. Duan, D. Jaksch, J. I. Cirac, and P. Zoller, “Dipole blockade and quantum information processing in mesoscopic atomic ensembles,” *Phys. Rev. Lett.* **87**, 037901 (2001).
- ³³K. R. Elder and M. Grant, “Modeling elastic and plastic deformations in nonequilibrium pro-

- cessing using phase field crystals,” *Phys. Rev. E* **70**, 051605 (2004).
- ³⁴H. Emmerich, H. Löwen, R. Wittkowski, T. Gruhn, G. Tóth, G. Tegze, and L. Gránásy, “Phase-field-crystal models for condensed matter dynamics on atomic length and diffusive time scales: An overview,” *Adv. Phys.* **61** (2012), 10.1080/00018732.2012.737555.
- ³⁵U. Thiele, A. J. Archer, M. J. Robbins, H. Gomez, and E. Knobloch, “Localized states in the conserved Swift-Hohenberg equation with cubic nonlinearity,” *Phys. Rev. E* **87**, 042915 (2013).
- ³⁶S. Sevinçli, N. Henkel, C. Ates, and T. Pohl, “Nonlocal nonlinear optics in cold Rydberg gases,” *Phys. Rev. Lett.* **107**, 153001 (2011).
- ³⁷F. Maucher, T. Pohl, S. Skupin, and W. Krolikowski, “Self-organization of light in optical media with competing nonlinearities,” *Phys. Rev. Lett.* **116**, 163902 (2016).
- ³⁸V. Heinonen, K. J. Burns, and J. Dunkel, “Quantum hydrodynamics for supersolid crystals and quasicrystals,” *Phys. Rev. A* **99**, 063621 (2019).
- ³⁹B. Krauskopf and H. M. Osinga, “Computing invariant manifolds via the continuation of orbit segments,” in *Numerical Continuation Methods for Dynamical Systems: Path following and boundary value problems*, edited by B. Krauskopf, H. M. Osinga, and J. Galán-Vioque (Springer Netherlands, Dordrecht, 2007) pp. 117–154.
- ⁴⁰S. Engelnkemper, S. V. Gurevich, H. Uecker, D. Wetzel, and U. Thiele, “Continuation for thin film hydrodynamics and related scalar problems,” in *Computational Modeling of Bifurcations and Instabilities in Fluid Mechanics*, Computational Methods in Applied Sciences, vol 50, edited by A. Gelfgat (Springer, Cham, 2019) pp. 459–501, <http://arxiv.org/abs/1808.02321>.
- ⁴¹U. Thiele, T. Frohoff-Hülsmann, S. Engelnkemper, E. Knobloch, and A. J. Archer, “First order phase transitions and the thermodynamic limit,” *New J. Phys.* **21**, 123021 (2019).
- ⁴²M. P. Holl, A. J. Archer, S. V. Gurevich, E. Knobloch, L. Ophaus, and U. Thiele, “Localized states in passive and active phase-field-crystal models,” *IMA J. Appl. Math.* **86**, 896–923 (2021).
- ⁴³J. Burke and E. Knobloch, “Localized states in the generalized Swift-Hohenberg equation,” *Phys. Rev. E* **73**, 056211 (2006).
- ⁴⁴P. Woods and A. Champneys, “Heteroclinic tangles and homoclinic snaking in the unfolding of a degenerate reversible Hamiltonian–Hopf bifurcation,” *Phys. D Nonlinear Phenom.* **129**, 147–170 (1999).
- ⁴⁵H. Uecker, D. Wetzel, and J. D. M. Rademacher, “pde2path - a matlab package for continuation and bifurcation in 2d elliptic systems,” *Numer. Math. Theor. Meth. Appl.* **7**, 58–106 (2014).
- ⁴⁶E. Gross, “Structure of a quantized vortex in boson systems,” *Nuovo Cim.* **20**, 454–477 (1961).

- ⁴⁷L. P. Pitaevskii, “Vortex lines in an imperfect Bose gas,” *Sov. Phys. JETP* **13**, 451 (1961).
- ⁴⁸The ansatz for the wave function is $\bar{\rho} + \varepsilon(v e^{i(\omega t - \mathbf{kx})} - w e^{-i(\omega t - \mathbf{kx})})$.
- ⁴⁹A. J. Archer, D. J. Ratliff, A. M. Rucklidge, and P. Subramanian, “Deriving phase field crystal theory from dynamical density functional theory: Consequences of the approximations,” *Phys. Rev. E* **100**, 022140 (2019).
- ⁵⁰W. Krolikowski, O. Bang, J. J. Rasmussen, and J. Wyller, “Modulational instability in nonlocal nonlinear Kerr media,” *Phys. Rev. E* **64**, 016612 (2001).
- ⁵¹E. Madelung, “Quantentheorie in hydrodynamischer Form,” *Z. Physik* **40**, 322–326 (1927).
- ⁵²R. Carles, R. Danchin, and J.-C. Saut, “Madelung, Gross-Pitaevskii and Korteweg,” *Nonlinearity* **25**, 2843–2873 (2012).
- ⁵³M. L. Chiofalo, S. Succi, and M. P. Tosi, “Ground state of trapped interacting Bose-Einstein condensates by an explicit imaginary-time algorithm,” *Phys. Rev. E* **62**, 7438–7444 (2000).
- ⁵⁴E. A. Donley, N. R. Claussen, S. L. Cornish, J. L. Roberts, E. A. Cornell, and C. E. Wieman, “Dynamics of collapsing and exploding bose–einstein condensates,” *Nature* **412**, 295–299 (2001).
- ⁵⁵F. Maucher, S. Skupin, and W. Krolikowski, “Collapse in the nonlocal nonlinear schrödinger equation,” *Nonlinearity* **24**, 1987–2001 (2011).
- ⁵⁶Actually, weakly nonlinear analysis shows (see section IV B and Appendix B below) that coexistence can be expected close to $\alpha_u = -1$ where the primary bifurcation can become subcritical. However, this parameter region is unphysical as one obtains negative densities.
- ⁵⁷Bifurcations for transition states between stripes and hexagons directly influence the amount of positive eigenvalues of the stripe solution. Fig. 12 shows that depending on the phase of the stripes the pattern resulting from such a transition might not have mirror symmetry with respect to the x -axis. As the latter is required by Neumann BC the corresponding bifurcation is then missed. Therefore, Neumann BC ultimately give rise to the artefact that stripes of different phase exhibit different stabilities.
- ⁵⁸M. P. Holl, A. J. Archer, and U. Thiele, “Efficient calculation of phase coexistence and phase diagrams: Application to a binary phase-field crystal model,” *J. Phys.: Condens. Matter* **33**, 115401 (2021).
- ⁵⁹J. D. Crawford, M. Golubitsky, M. G. M. Gomes, E. Knobloch, and I. M. Stewart, “Boundary conditions as symmetry constraints,” in *Singularity Theory and its Applications, Part II*, Lecture Notes in Mathematics, Vol. 1463 (Springer, New York, 1991) pp. 63–79.

- ⁶⁰A. J. Archer, M. C. Walters, U. Thiele, and E. Knobloch, “Solidification in soft-core fluids: Disordered solids from fast solidification fronts,” *Phys. Rev. E* **90**, 042404 (2014).
- ⁶¹A. R. P. Lima and A. Pelster, “Quantum fluctuations in dipolar Bose gases,” *Phys. Rev. A* **84**, 041604 (2011).
- ⁶²Y.-C. Zhang, F. Maucher, and T. Pohl, “Supersolidity around a critical point in dipolar Bose-Einstein condensates,” *Phys. Rev. Lett.* **123**, 015301 (2019).
- ⁶³Y.-C. Zhang, T. Pohl, and F. Maucher, “Phases of supersolids in confined dipolar Bose-Einstein condensates,” *Phys. Rev. A* **104**, 013310 (2021).
- ⁶⁴J. Hertkorn, J.-N. Schmidt, M. Guo, F. Böttcher, K. S. H. Ng, S. D. Graham, P. Uerlings, T. Langen, M. Zwierlein, and T. Pfau, “Pattern formation in quantum ferrofluids: From supersolids to superglasses,” *Phys. Rev. Research* **3**, 033125 (2021).
- ⁶⁵R. Hoyle, *Pattern Formation: An Introduction to Methods*, repr. ed. (Cambridge Univ. Press, Cambridge [u.a.], 2007).
- ⁶⁶L. Landau, “On the theory of phase transitions,” *Zh. Eksp. Teor. Fiz.* **7**, 19 (1937).
- ⁶⁷A. B. Steinberg, F. Maucher, S. V. Gurevich, and U. Thiele, “Data supplement for ‘Exploring bifurcations in Bose-Einstein condensates via phase field crystal models’,” 10.5281/zenodo.6594198 (2022).